Operational stability, low light performance, and long-lived transients in mixed-halide perovskite solar cells with a monolayer-based hole extraction layer

Richard Murdey[*,1], Yasuhisa Ishikura[2], Yuko Matsushige[1], Shuaifeng Hu[1], Jorge Pascual[1], Minh Anh Truong[1], Tomoya Nakamura[1], Atsushi Wakamiya[1]

[1]Institute for Chemical Research, Kyoto University, Gokasho, Uji, Kyoto 611-0011, Japan

[2]Enecoat Technologies, Co. Ltd., Sakosotoyashiki 43-1, Kumiyama, Kuse, Kyoto 613-0031, Japan

*Corresponding author

E-mail address: *murdey@scl.kyoto-u.ac.jp* (R. Murdey)

Keywords

Perovskite solar cells, Self-assembled monolayers, Bandgap, Stability, Ambient light harvesting

Abstract

Due to their tunable bandgap and low manufacturing cost, metal halide perovskite solar cells are attractive for ambient/indoor light-harvesting applications. In this work, we evaluate p-i-n perovskite solar cells fabricated with MeO-2PACz, a molecular monolayer hole extraction layer, as potential candidates for ambient light-harvesting applications. Two triple-cation mixed halide lead perovskite absorbers are compared, one with high bromide content (Br/I ratio 1:2, bandgap 1.72 eV, 16.1% power conversion efficiency) and one with low bromide content (Br/I ratio 1:11, bandgap 1.57 eV, 19.1% power conversion efficiency). Both materials demonstrated good stability while operating under simulated sunlight at the maximum power point for 100 h, a cumulative light dose comparable to over two years of ambient use. After 100 h operation, however, the measured device efficiency fell temporarily due to a transient loss of output current before returning to the nominal level after a long recovery period in the dark. These transient losses were more apparent in the wide bandgap device under strong light and were likely caused by light-induced halide segregation. After recovery, both devices retained good performance under a wide range of light intensities. Under a simulated ambient light source (835 lx white LED), the power conversion efficiency of the wide bandgap device reached 30.4%.

1. Introduction

Solar cells based on metal halide perovskite materials have demonstrated exceptional efficiency (25.7%), approaching that of crystalline silicon.[1] The perovskite absorber layers have many favorable electro-optic properties, including high defect tolerance,[2] long charge carrier lifetimes and diffusion lengths,[3,4] and high absorption coefficients.[5] One particularly useful feature is the ability to tune the bandgap by substituting different ions in the perovskite crystal structure.[6,7] The bandgap of these mixed composition perovskites can be optimized for use in tandem cells,[8–11] or cells designed to operate efficiently under artificial light sources.[12] In combination with the low manufacturing cost, the high potential efficiency of wide-bandgap perovskite solar cells under artificial light makes them highly promising for powering small, low-power devices such as remote sensors, RFID tags, and Bluetooth Low Energy (BLE) beacons.[13]

The bandgap of metal halide perovskites can be adjusted over a wide range by varying the ratio of halide ions, normally iodide and bromide, occupying the X-site of the ABX_3 crystal structure.[14,15] The ratio of the A-site cations, typically a mix of cesium (Cs^+), formamidinium (FA^+), and methylammonium (MA^+), is optimized to increase the stability and/or improve the electrical properties of the perovskite.[16,17] Increasing the bandgap via the halide ratio has limitations, however. As the Br/I ratio is increased, stability and performance can be compromised by the tendency for the I^- and Br^- ions to separate into distinct phases when the perovskite is illuminated.[18,19] This transient diffusion phenomenon – the halide distribution returns to a homogeneous mixture in the dark – is known as halide segregation.[20–23]

In this work, we focused on a p-i-n or "inverted" device structure employing a carbazole-based self-assembled monolayer (SAM) as a hole extraction layer. Record efficiencies for both single junction and tandem solar cells have been recently achieved by coating the transparent oxide substrates with these molecular monolayers.[24–26] It has also been reported that perovskite layers deposited on SAM-treated substrates are resilient toward halide segregation.[24] We wanted to explore the stability and performance of the monolayer-based device stack with both wide and narrow gap absorbers. To this end, we prepared devices using mixed-halide perovskites with different bromide-to-iodide ratios. One material has a narrow bandgap optimal for natural sunlight, the other has a wide bandgap suitable for ambient light-harvesting or tandem applications. Operational stability was assessed by tracking the maximum output power for 100 h under AM1.5G simulated sunlight, a total light flux equivalent to over two years of operation under typical indoor lighting conditions. While the efficiency of both the narrow and wide gap devices remained above the initial value throughout the test, significant transient losses were

observed after the test was completed. These long-lived transients, which act to suppress the responsivity of the device under strong light, were more apparent when the wide-bandgap perovskite with high bromide content was used as the absorber layer. The initial performance could be recovered after storing the devices in the dark. After recovery, both devices retained good performance under low light conditions. Finally, the wide bandgap device was confirmed to operate efficiently under simulated ambient light. In addition to quantifying the stability and efficiency of the SAM-based device structure for ambient light harvesting, our results provide insights into the influence of perovskite bandgap and composition on the operational stability, low light performance, and transient behavior of monolayer-based p-i-n perovskite solar cells.

2. Results

2.1 Device fabrication and test conditions

For the low bromide content (low-Br) material we selected our $Cs_{0.05}FA_{0.80}MA_{0.15}PbI_{2.75}Br_{0.25}$ reference composition.[27] The ratio of bromide to iodide is 1:11 (8.3% of the total halide content is bromide), and the bandgap of 1.57 eV (787 nm) is optimized for single junction performance under AM1.5G sunlight. For the high bromide content (high-Br) formulation we used $Cs_{0.05}FA_{0.80}MA_{0.15}PbI_2Br$. The bromide to iodide ratio is 1:2 (33% bromide), resulting in a wider bandgap of 1.72 eV (722 nm). This wide-bandgap absorber is expected to perform well under ambient lighting such as white LEDs. The composition of the A-site is kept unchanged. The hole extracting monolayer was made with a carbazole-based SAM molecule, [2-(3,6-dimethoxy-9H-carbazol-9-yl)ethyl]phosphonic acid (MeO-2PACz, molecular structure shown in **Fig. 1a**), which was applied to indium tin oxide (ITO)/glass substrates by spin coating from 1 mM ethanol solution.[28] Perovskite solar cells were fabricated on the SAM-treated ITO glass substrates based on the processes elaborated in our previous reports[29–31] and outlined in the supporting information. Each device had an active (masked) area of 0.1 cm^2. The complete device structure, illustrated in **Fig. 1b**, is ITO/MeO-2PACz/perovskite/C_{60}/BCP/Ag. Cross-sectional SEM images (**Fig. S1**) confirm the perovskite layers in both devices to be about 600 nm thick, with comparable grain size and morphology. While the devices were exposed briefly to air to apply solder to the electrode contacts, they were otherwise kept under an inert atmosphere for the duration of the work. All tests and measurements were performed at ambient temperature.

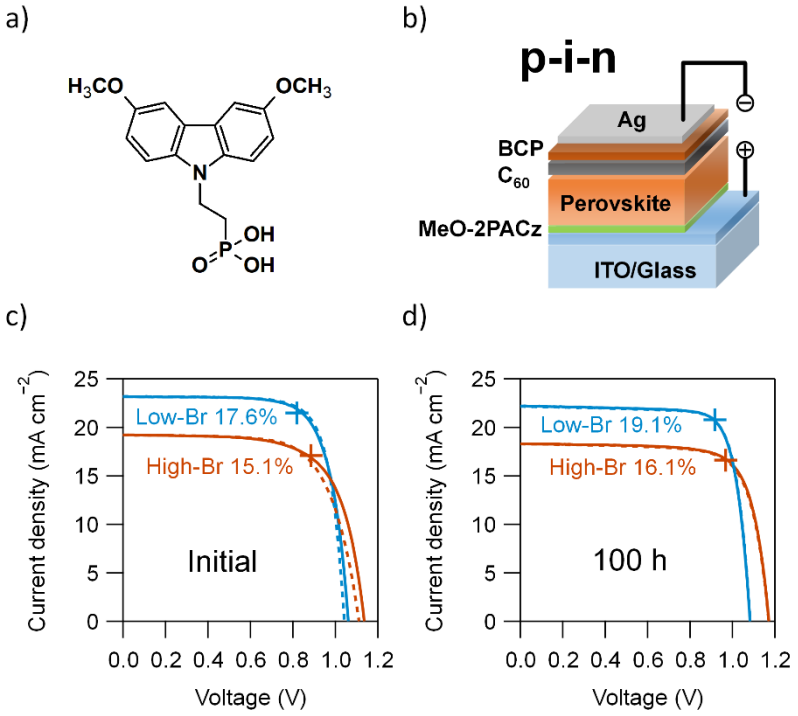

Fig. 1. (a) Chemical structure of the MeO-2PACz SAM molecule. (b) Structure of the p-i-n perovskite solar cells used in this work. (c) Forward (solid line) and reverse (dashed line) *J*–*V* curves and stabilized operating points (cross marks) for the devices (c) in their initial state and (d) after 100 h operation under AM1.5G. Low-Br: $Cs_{0.05}FA_{0.80}MA_{0.15}PbI_{2.75}Br_{0.25}$ perovskite (Br/I ratio 1:11, bandgap 1.57 eV). High-Br: $Cs_{0.05}FA_{0.80}MA_{0.15}PbI_2Br$ perovskite (Br/I ratio 1:2, bandgap 1.72 eV).

2.2 Device performance

Stabilized output and current–voltage (*J*–*V*) curves for representative low-Br and high-Br devices are shown in **Fig. 1c**. Under AM1.5G, the power conversion efficiency (PCE) for the low-Br device was 17.6%, while that of the high-Br device was 15.1%. The lower PCE of the high-Br device under AM1.5G is expected considering the wider bandgap, as less light energy is absorbed. The difference in bandgap leads to the high-Br device having a lower observed short circuit current (J_{sc}) and higher open circuit voltage (V_{oc}) compared to the low-Br device.

Fig. 1d shows stabilized output and current–voltage (*J*–*V*) curves for the same devices after 100 h operation at the maximum power point under AM1.5G. The characteristics of both cells improved: The stabilized PCE of the low-Br device reached 19.1%, while that of the high-

Br device increased to 16.1%. While the short circuit currents decreased slightly, the open circuit voltages increased to 1.08 V and 1.17 V, respectively. The fill factors (FF) also increased. The FF of the low-Br device remained slightly higher than that of the high-Br counterpart, at 0.79 and 0.76, respectively.

The output characteristics before and after operation for 100 h are compiled in **Table 1**.

Table 1. Devices characteristics before and after 100 h operation under AM1.5G.

Cell	Scan Direction	J_{sc} (mA cm^{-2})	V_{oc} (V)	PCE[a] (%)	FF	PCE[b] (%)
Low-Br (Initial)	Forward	23.14	1.06	18.2	0.74	17.6
	Reverse	23.16	1.04	18.5	0.76	
Low-Br (100 h)	Forward	22.19	1.08	19.0	0.79	19.1
	Reverse	22.13	1.08	19.0	0.79	
High-Br (Initial)	Forward	19.22	1.14	15.0	0.69	15.1
	Reverse	19.20	1.11	14.6	0.69	
High-Br (100 h)	Forward	18.34	1.17	16.2	0.76	16.1
	Reverse	18.30	1.17	16.1	0.75	

[a] Calculated from the *J–V* scans

[b] Stabilized measurement after at least 300 s maximum power point tracking

2.3 Operational stability

In this section, we present the evolution of the device properties during 100 h operation under AM1.5G. The maximum power point tracking (MPPT) algorithm which kept the devices at the maximum output power, p_m, was paused for brief intervals every 20 minutes to record *J–V* curves. The progression of J_{sc}, V_{oc}, and FF was obtained from the *J–V* curves, while the PCE is taken directly from the MPPT data. The results are compiled in **Fig. 2**, while representative *J–V* scans at 1, 10, and 100 h are shown in **Fig. S2**. V_{oc} and FF increased over the 100-h test interval for both the low-Br and high-Br devices, while J_{sc} fell slightly. The increase in voltage and fill factor offsets the decrease in output current such that the overall efficiency of both cells after 100 h MPPT remained higher than the initial value. The PCE increased and reached a maximum value at about 25 h. This "burn-in" behavior has been previously noted as a characteristic of p-i-n perovskite solar cells, though the exact cause is not known.[32] Given the improvements in output voltage over the burn-in period and the noted sensitivity of p-i-n monolayer devices to modification of the perovskite/C_{60} interface,[33,34] this interface may become naturally passivated as the device ages over the initial hours of operation. In sharp contrast, considerable

degradation was observed when the perovskite materials were tested in n-i-p devices with spiro-OMeTAD hole transport layers. These results confirm the superior operational stability of the monolayer-based p-i-n device stack for both the wide and narrow bandgap perovskite absorber layers. The 100 h MPPT data for the spiro-OMeTAD-based devices is given in **Fig. S3**.

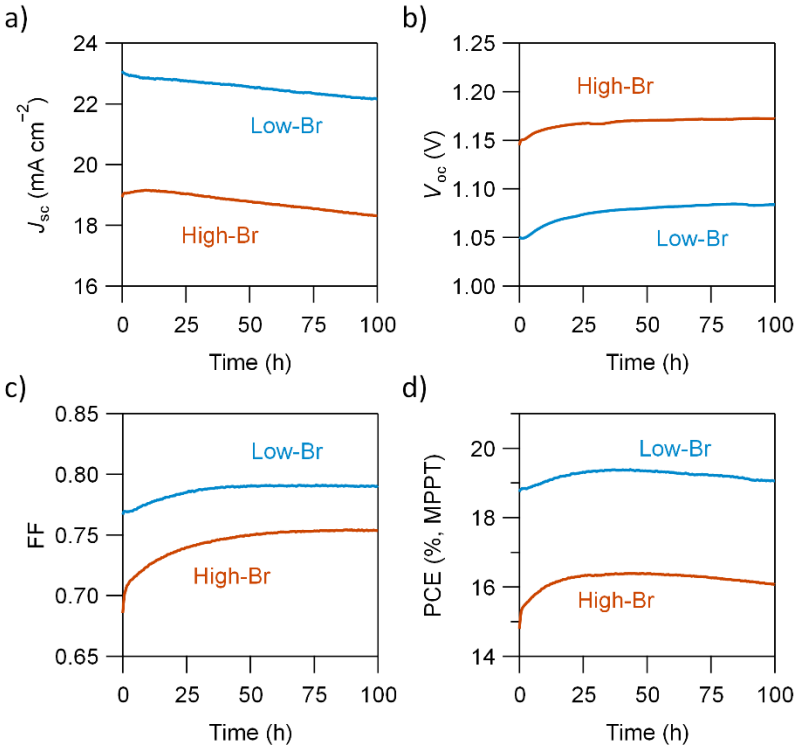

Fig. 2. Electrical performance of the solar cells while operating at maximum power for 100 h. (a) J_{sc}, (b) V_{oc}, (c) FF, and (d) PCE. The PCE is determined directly from the MPPT data, while the remaining parameters are derived from *J*–*V* curves recorded during the MPPT run at 20-minute intervals.

2.4 Transient effects

The devices showed good stability during the 100-h operational test under continuous AM1.5G, with only minor changes to the *J*–*V* curves and minimal net loss of PCE. We were therefore surprised to see a sharp drop in output current when, following the completion of the test, the devices were subsequently left under ambient room light for a short period (<1 h). This loss was transient, however, and the nominal performance was recovered after the device was left in the dark for a longer period (500 h). These transient effects were more pronounced for the high-Br device than the low-Br device. The details of the transient effect for the high-Br device are explored in **Fig. 3**.

As illustrated by the *J*–*V* curves in **Fig. 3a**, an acute performance drop develops after the MPPT test is completed and the device was left for an hour or so in the dark. J_{sc} fell from 18.3 mA cm^{-2} to about 12 mA cm^{-2}, before returning to 18.7 mA cm^{-2} after a 500-h recovery period in the dark. We noted, however, that the magnitude of the transient loss was greatly reduced when the device was probed with low-intensity light. To help characterize this interesting previously unremarked phenomenon, it is instructive to examine J_{sc} normalized to the incident light power. This quantity is known as the responsivity of the device, $\mathcal{R} = J_{sc}/\varphi$ (φ is the irradiance). The responsivity is shown plotted against light intensity in **Fig. 3b**. Although the responsivity remained essentially constant over the measured range of light intensities in the initial and recovered states, in the transient state the responsivity falls with increasing light intensity from about 1/100 sun. The responsivity below 1/100 was unchanged from the initial and recovered values, however, so the impact of the transient effects under ambient light is expected to be minimal.

External quantum efficiency (EQE) spectra, shown in **Fig. 3c**, were taken to help clarify the transient changes. All three of the measured spectra – taken for the initial, transit, and recovered states – show the same overall EQE of 80–85%. The measured EQE is not lower during the transient regime because the intensity of the monochromatic light source used for this experiment corresponds to only about 1/100 sun – the threshold below which, as noted above, the transient loss of responsivity ceases to be significant. Although the spectral shape and intensity are unchanged, the onset region temporarily developed a low-energy shoulder during the transient regime which dissipated after recovery. This is more clearly seen in **Fig. 3d**, where the differential of the EQE signal is plotted against photon energy. Following the procedures developed by U. Rau et al., the bandgap is estimated from the peak centers determined from Gaussian curve fitting.[35] As listed in **Table 2**, the bandgap of the high-Br material shifts from 1.717 to 1.699

eV before returning to 1.717 eV, and the peak width increases from 83 to 110 meV before returning to 85 meV. Interpolating the bandgap and bromide content of the two perovskite materials, the shift in the bandgap of the high-Br device suggests a reduction in bromide content from 0.33% to 0.30%. In other words, the regions of the perovskite layer where light is most strongly absorbed become temporarily iodide rich. This is consistent with the previously reported segregation of the halide ions into Br-rich and I-rich subdomains under strong light.[22,23,36–38] Light-induced lattice expansion at the illuminated perovskite surface seems the likely driving force.[39–42] It's noteworthy though that in the present instance the detrimental influence of the halide segregation on device performance is exhibited *after* exposure to AM1.5G rather than *during* it.

Significant structural changes within the perovskite layer are deduced from the X-ray diffraction (XRD) measurements shown in **Fig. S4**. A high-Br perovskite thin film was prepared on a MeO-2PACz coated ITO substrate and exposed to AM1.5G for 100 h. (Mirroring the MPPT experiments, the perovskite was exposed from the ITO side.) A significant shift of all the perovskite diffraction peaks to lower 2θ values was observed following light exposure, accompanied by an overall broadening. Following the previous report, we interpret this as a light- or temperature-induced heterogenous expansion of the perovskite lattice.[43] The diffraction patterns were unchanged for at least several hours after illumination ceased, and began to show clear signs of recovery after 24 h in the dark. It seems likely that the drop in current responsivity in the high-Br device and its gradual recovery in the dark is related to this lattice expansion, which also coincides with the halide segregation induced shift in the perovskite bandgap determined from the EQE measurements. While lattice expansion and phase segregation are probably both contributing factors, more research is needed to determine the role of the p-i-n device stack, and in particular the influence of the MeO-2PACz monolayer, in driving or suppressing the transient changes in responsivity.

While similar changes in device responsivity and output current were observed for the low-Br device (**Fig. S5**) the loss of output current was much smaller and there was no corresponding shift in the onset of the EQE spectrum. These transients were similarly recovered after 500 h in the dark. The contrasting behavior for the high-Br and low-Br devices establishes further evidence that the transient effect is related to halide segregation. We also briefly checked the transient behavior of the high-Br perovskite absorber in a p-i-n device where the MeO-2PACz monolayer HEL was replaced by PTAA. The operational stability is lower than the MeO-2PACz devices, as shown in **Fig. S6**. This agrees with an earlier study.[44] While a similar shift in

bandgap was observed from the EQE data after 100 h MPPT, there was no transient loss of device current following the MPPT experiment. Instead, the device performance further degraded in the days following the MPPT experiment, with no indication of recovery.

Impedance measurements tell a different story, however. Irreversible changes in both devices were observed in the complex impedance spectra recorded under AM1.5G (**Fig. S7** and **Appendix A**). The parallel resistance[45] falls over the course of the MPPT experiment and does not return to the initial state even after 500 h recovery. The effective shunt resistance remains high, however, and the impact of the change on the measured device performance (as expressed by the *J*–*V* curves and MPPT under AM1.5G) should be negligible.

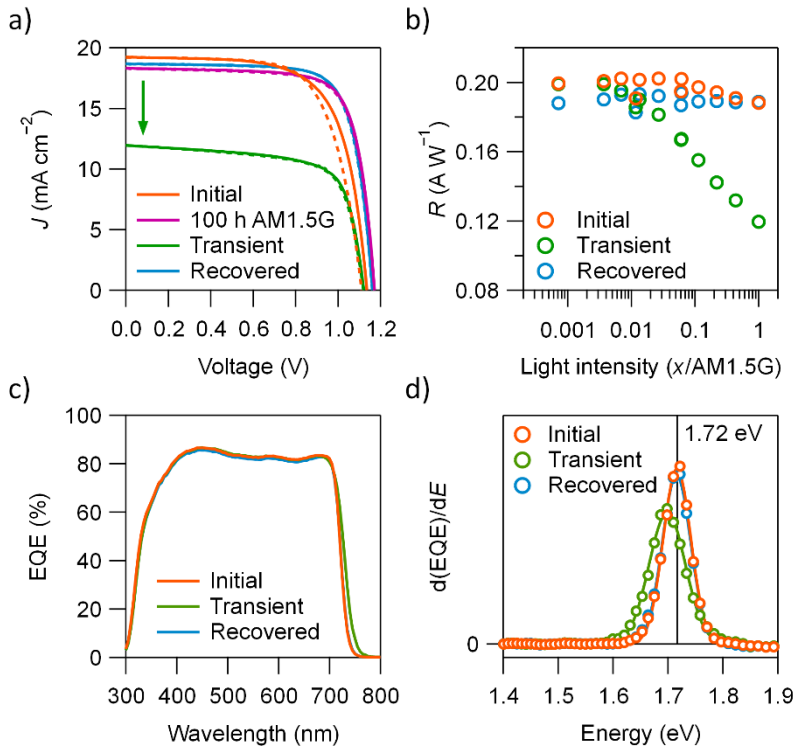

Fig. 3. Properties of the high-Br device before (Initial) and after the 100 h MPPT test (100 h AM1.5G), in the hours following 100 h MPPT (Transient), and after 500 h in dark storage (Recovered). (a) Forward (solid line) and reverse (dashed line) *J*–*V* curves under AM1.5G show the significant loss of J_{sc} in the hours following 100 h MPPT. (b) Corresponding loss of device responsivity as a function of light intensity. (c) EQE spectra. (d) The differential of the EQE signal around the onset region. Gaussian curve fits of the experimental data points are indicated as solid lines.

Table 2. Gaussian peak fitting results for the derivative of the external quantum efficiency, d(EQE)/d*E*.

Condition	Low-Br		High-Br	
	Position (eV)	FWHM (eV)	Position (eV)	FWHM (eV)
Initial	1.574	0.068	1.717	0.083
Transient	1.576	0.070	1.699	0.110
Recovered	1.574	0.068	1.716	0.085

2.5 Light intensity dependence

Light intensity dependence tests and performance evaluation under ambient light were performed on cells previously stressed with 100 h operation at maximum power under AM1.5G, after full recovery from the transient effects described above. During these tests, the cells absorb a photon flux equivalent to over two years of continuous operation under ambient light. The results presented here are therefore indicative of how these devices, provided sufficient protection from the atmosphere, might perform after several years of operation in a typical Internet of Things application.

To arrive at a clearer picture of how the performance of these stressed cells change under different light intensities, simulated AM1.5G radiation was attenuated using neutral density filters in combination with a variable aperture. (Calibration methods are given in the supporting information.) By keeping the spectral composition constant, direct comparison of the PCE data is possible across a range of light intensity – something that would not have been possible if, for example, we had switched to a LED source for the low light measurements. **Fig. 4a** shows the PCE of the low-Br and high-Br devices as the AM1.5G source is attenuated from 1 sun to less than 1/1000 suns. The PCE is calculated from the average of forward and reverse *J*–*V* curves recorded at each light intensity. (Full datasets are given in **Appendix B** of the supporting information.) The Shockley–Queisser (SQ) limit for the two materials is also indicated. While the output from both devices is lower under low light, the SQ limit also falls as the light intensity is reduced. At any given light intensity, both devices perform equally strongly vs. their respective theoretical limits. This can be clearly seen in the plot of the cell output normalized to the SQ limit shown in **Fig. S8**.

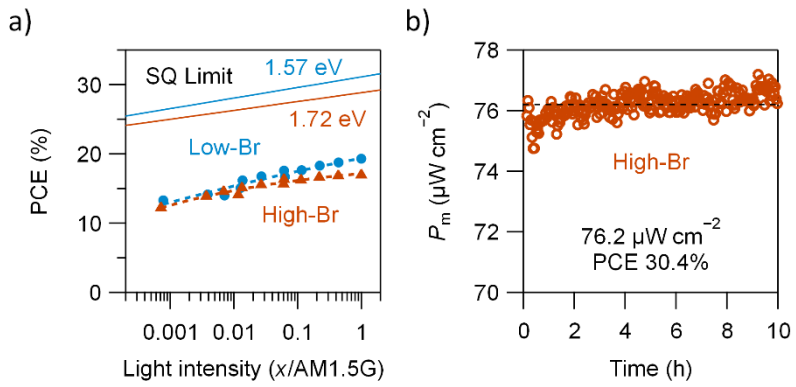

Fig. 4. (a) Cell efficiencies for the devices under attenuated AM1.5G light. The estimated SQ limit for both materials based on their respective bandgaps is indicated by the solid lines, while polynomial fits of the experimental data (dashed lines) emphasize the relative curvature. (b) Maximum power output ($P_{m,\ MPPT}$) of the high-Br device under white LED illumination (250 µW/cm^2, 835 lx) simulating ambient lighting conditions. The device was kept in the dark overnight before measurements began.

2.6 Device characteristics under simulated ambient light

Having established that both materials retain the same performance relative to their respective SQ limits under attenuated AM1.5G, we could confirm the stable output of the widegap high-Br composition under simulated ambient indoor light. A 50 W white LED adjusted to an irradiance of 250 µW cm^{-2} – illuminance 835 lx, roughly the brightness of a normal office environment – was used to simulate ambient light conditions. As shown in **Fig. S9**, the spectral intensity is mostly restricted to between 430–700 nm. As shown in **Fig. S10**, the absence of any significant infrared component imparts an efficiency advantage to absorbers with wide bandgaps in the region of 1.7–1.9 eV, including the high-Br perovskite studied in this work.

Fig. 4b shows the maximum power output of the high-Br device under the white LED. The cell was kept in the dark overnight before the measurements started. The average output of the high-Br cell during 10 h of operation was 76.2 µW cm^{-2}, corresponding to a PCE of 30.4%. This efficiency, while promising, might be increased by changing the halide composition to slightly increase the bandgap of the perovskite absorber, [46] or by reducing charge carrier recombination at the perovskite/ETL interface using 2D capping layers.[34]

3. Conclusion

The performance and stability of p-i-n perovskite solar cells using MeO-2PACz as a hole extracting monolayer were examined with a focus on ambient light-harvesting applications. During this work, we also clarified the influence of the perovskite bromide-to-iodide ratio on device performance. Two different mixed halide perovskite absorbers were trialed, a low-Br material (Br/I 1:11) with a bandgap of 1.57 eV and a high-Br formulation (Br/I 1:2) with a bandgap of 1.72 eV well-suited for operation under artificial light sources such as LEDs. We found that the devices maintain high PCE during 100 h operation at maximum power under AM1.5G. Transient losses were observed after the MPPT tests were completed, however. The transient changes are attributed to halide segregation and dissipated after the devices were stored in the dark for 500 h. Fortunately, given the intended application in ambient light harvesting, the effect of the transient changes on the device performance in low light was found to be negligible. After recovery, the performance of both materials closely tracked their respective SQ limits over a wide range of incident light intensities from less than 1/1000 sun to 1 sun. Under low-intensity white LED illumination (835 lx) the wide bandgap, high-Br perovskite material achieved a stable PCE of 30.4%. Overall, we conclude that the monolayer-based p-i-n device structure with wide bandgap perovskite absorber layers shows great promise for long-term deployment in ambient-light harvesting applications from the standpoint of both efficiency and operational stability.

Acknowledgments

This research was partially supported by the Ministry of Education, Culture, Sports, Science and Technology, Grant-in-Aid for Scientific Research (C), JSPS KAKENHI (grant numbers JP19K05666, JP19K23631, and JP20K22531), grant-in-Aid for Early-Career Scientists (21K14694), and by JST-COI (grant number JPMJCE 1307). Additional funding was provided by the New Energy and Industrial Technology Development Organization (NEDO), and research grants from the Tokyo Ohka Foundation for the Promotion of Science and Technology, the Sumitomo Foundation, and the Mazda Foundation. The authors thank K. Aihara of Citizen Co for helpful discussions and Y. Iwasaki for performing the SEM measurements. Finally, we gratefully acknowledge N. Kurose and N. Shioya for their assistance with the X-ray diffraction experiments.

ORCID

Richard Murdey: 0000-0001-7621-9664

Shuaifeng Hu: 0000-0003-1312-075X

Jorge Pascual: 0000-0001-6486-0737

Minh Anh Truong: 0000-0003-2649-0282

Tomoya Nakamura: 0000-0001-7059-931X

Atsushi Wakamiya: 0000-0003-1430-0947

References

[1] NREL Efficiency Chart, (n.d.).

[2] R.E. Brandt, J.R. Poindexter, P. Gorai, R.C. Kurchin, R.L.Z. Hoye, L. Nienhaus, M.W.B. Wilson, J.A. Polizzotti, R. Sereika, R. Žaltauskas, L.C. Lee, J.L. Macmanus-Driscoll, M. Bawendi, V. Stevanović, T. Buonassisi, Searching for "defect-Tolerant" Photovoltaic Materials: Combined Theoretical and Experimental Screening, Chemistry of Materials. 29 (2017) 4667–4674. https://doi.org/10.1021/acs.chemmater.6b05496.

[3] C. Wehrenfennig, G.E. Eperon, M.B. Johnston, H.J. Snaith, L.M. Herz, High charge carrier mobilities and lifetimes in organolead trihalide perovskites, Advanced Materials. 26 (2014) 1584–1589. https://doi.org/10.1002/adma.201305172.

[4] L.M. Herz, Charge-Carrier Mobilities in Metal Halide Perovskites: Fundamental Mechanisms and Limits, ACS Energy Letters. 2 (2017) 1539–1548. https://doi.org/10.1021/acsenergylett.7b00276.

[5] S. de Wolf, J. Holovsky, S.J. Moon, P. Löper, B. Niesen, M. Ledinsky, F.J. Haug, J.H. Yum, C. Ballif, Organometallic halide perovskites: Sharp optical absorption edge and its relation to photovoltaic performance, Journal of Physical Chemistry Letters. 5 (2014) 1035–1039. https://doi.org/10.1021/jz500279b.

[6] G.E. Eperon, S.D. Stranks, C. Menelaou, M.B. Johnston, L.M. Herz, H.J. Snaith, Formamidinium lead trihalide: A broadly tunable perovskite for efficient planar heterojunction solar cells, Energy and Environmental Science. 7 (2014) 982–988. https://doi.org/10.1039/c3ee43822h.

[7] J.H. Noh, S.H. Im, J.H. Heo, T.N. Mandal, S. il Seok, Chemical management for colorful, efficient, and stable inorganic-organic hybrid nanostructured solar cells, Nano Letters. 13 (2013) 1764–1769. https://doi.org/10.1021/nl400349b.

[8] D.P. McMeekin, G. Sadoughi, W. Rehman, G.E. Eperon, M. Saliba, M.T. Hörantner, A. Haghighirad, N. Sakai, L. Korte, B. Rech, M.B. Johnston, L.M. Herz, H.J. Snaith, M.T. Horantner, A. Haghighirad, N. Sakai, L. Korte, B. Rech, M.B. Johnston, L.M. Herz, H.J. Snaith, A mixed-cation lead mixed-halide perovskite absorber for tandem solar cells, Science (1979). 351 (2016) 151–155. https://doi.org/10.1126/science.aad5845.

[9] T. Leijtens, K.A. Bush, R. Prasanna, M.D. McGehee, Opportunities and challenges for tandem solar cells using metal halide perovskite semiconductors, Nature Energy. 3 (2018) 828–838. https://doi.org/10.1038/s41560-018-0190-4.

[10] D. Kim, H.J. Jung, I.J. Park, B.W. Larson, S.P. Dunfield, C. Xiao, J. Kim, J. Tong, P. Boonmongkolras, S.G. Ji, F. Zhang, S.R. Pae, M. Kim, S.B. Kang, V. Dravid, J.J. Berry, J.Y. Kim, K. Zhu, D.H. Kim, B. Shin, Efficient, stable silicon tandem cells enabled by anion-engineered wide-bandgap perovskites, Science (1979). 160 (2020) eaba3433. https://doi.org/10.1126/science.aba3433.

[11] N.J. Jeon, J.H. Noh, W.S. Yang, Y.C. Kim, S. Ryu, J. Seo, S. il Seok, Compositional engineering of perovskite materials for high-performance solar cells, Nature. 517 (2015) 476–480. https://doi.org/10.1038/nature14133.

[12] X. He, J. Chen, X. Ren, L. Zhang, Y. Liu, J. Feng, J. Fang, K. Zhao, S. Liu, 40.1% Record Low-Light Solar-Cell Efficiency by Holistic Trap-Passivation using Micrometer-Thick Perovskite Film, Advanced Materials. 2100770 (2021) 1–10. https://doi.org/10.1002/adma.202100770.

[13] S.N.R. Kantareddy, I.M. Peters, I. Mathews, S. Sun, M. Layurova, J. Thapa, J.P. Correa-Baena, R. Bhattacharyya, T. Buonassisi, S.E. Sarma, Perovskite PV-Powered RFID: Enabling Low-Cost Self-Powered IoT Sensors, IEEE Sensors Journal. 20 (2020) 471–478. https://doi.org/10.1109/JSEN.2019.2939293.

[14] T. Jesper Jacobsson, J.-P. Correa-Baena, M. Pazoki, M. Saliba, K. Schenk, M. Grätzel, A. Hagfeldt, Exploration of the compositional space for mixed lead halogen perovskites for high efficiency solar cells, Energy & Environmental Science. 9 (2016) 1706–1724. https://doi.org/10.1039/C6EE00030D.

[15] J.-P. Correa-Baena, M. Saliba, T. Buonassisi, M. Grätzel, A. Abate, W. Tress, A. Hagfeldt, Promises and challenges of perovskite solar cells, Science (1979). 358 (2017) 739–744. https://doi.org/10.1126/science.aam6323.

[16] M. Saliba, J.-P. Correa-Baena, C.M. Wolff, M. Stolterfoht, N. Phung, S. Albrecht, D. Neher, A. Abate, How to Make over 20% Efficient Perovskite Solar Cells in Regular (n–i–p) and Inverted (p–i–n) Architectures, Chemistry of Materials. 30 (2018) 4193–4201. https://doi.org/10.1021/acs.chemmater.8b00136.

[17] M. Saliba, T. Matsui, J.-Y. Seo, K. Domanski, J.-P. Correa-Baena, M.K. Nazeeruddin, S.M. Zakeeruddin, W. Tress, A. Abate, A. Hagfeldt, M. Grätzel, Cesium-containing triple cation perovskite solar cells: improved stability, reproducibility and high efficiency, Energy & Environmental Science. 9 (2016) 1989–1997. https://doi.org/10.1039/C5EE03874J.

[18] T. Duong, H.K. Mulmudi, Y. Wu, X. Fu, H. Shen, J. Peng, N. Wu, H.T. Nguyen, D. Macdonald, M. Lockrey, T.P. White, K. Weber, K. Catchpole, Light and Electrically Induced Phase Segregation and Its Impact on the Stability of Quadruple Cation High Bandgap Perovskite Solar Cells, ACS Applied Materials and Interfaces. 9 (2017) 26859–26866. https://doi.org/10.1021/acsami.7b06816.

[19] J. Xu, C.C. Boyd, Z.J. Yu, A.F. Palmstrom, D.J. Witter, B.W. Larson, R.M. France, J. Werner, S.P. Harvey, E.J. Wolf, W. Weigand, S. Manzoor, M.F.A.M.A.M. van Hest, J.J. Berry, J.M. Luther, Z.C. Holman, M.D. McGehee, Triple-halide wide–band gap perovskites with suppressed phase segregation for efficient tandems, Science (1979). 367 (2020) 1097–1104. https://doi.org/10.1126/science.aaz5074.

[20] E.T. Hoke, D.J. Slotcavage, E.R. Dohner, A.R. Bowring, H.I. Karunadasa, M.D. McGehee, Reversible photo-induced trap formation in mixed-halide hybrid perovskites for photovoltaics, Chemical Science. 6 (2015) 613–617. https://doi.org/10.1039/c4sc03141e.

[21] A.J. Barker, A. Sadhanala, F. Deschler, M. Gandini, S.P. Senanayak, P.M. Pearce, E. Mosconi, A.J. Pearson, Y. Wu, A.R. Srimath Kandada, T. Leijtens, F. de Angelis, S.E. Dutton, A. Petrozza, R.H. Friend, Defect-Assisted Photoinduced Halide Segregation in Mixed-Halide Perovskite Thin Films, ACS Energy Letters. 2 (2017) 1416–1424. https://doi.org/10.1021/acsenergylett.7b00282.

[22] M.C. Brennan, S. Draguta, P. v. Kamat, M. Kuno, Light-Induced Anion Phase Segregation in Mixed Halide Perovskites, ACS Energy Letters. 3 (2018) 204–213. https://doi.org/10.1021/acsenergylett.7b01151.

[23] D.J. Slotcavage, H.I. Karunadasa, M.D. McGehee, Light-Induced Phase Segregation in Halide-Perovskite Absorbers, ACS Energy Letters. 1 (2016) 1199–1205. https://doi.org/10.1021/acsenergylett.6b00495.

[24] A. Al-Ashouri, E. Köhnen, B. Li, A. Magomedov, H. Hempel, P. Caprioglio, J.A. Márquez, A.B. Morales Vilches, E. Kasparavicius, J.A. Smith, N. Phung, D. Menzel, M. Grischek,

L. Kegelmann, D. Skroblin, C. Gollwitzer, T. Malinauskas, M. Jošt, G. Matič, B. Rech, R. Schlatmann, M. Topič, L. Korte, A. Abate, B. Stannowski, D. Neher, M. Stolterfoht, T. Unold, V. Getautis, S. Albrecht, Monolithic perovskite/silicon tandem solar cell with >29% efficiency by enhanced hole extraction, Science (1979). 370 (2020) 1300–1309. https://doi.org/10.1126/science.abd4016.

[25] Y. Lin, A. Magomedov, Y. Firdaus, D. Kaltsas, A. El-Labban, H. Faber, D.R. Naphade, E. Yengel, X. Zheng, E. Yarali, N. Chaturvedi, K. Loganathan, D. Gkeka, S.H. AlShammari, O.M. Bakr, F. Laquai, L. Tsetseris, V. Getautis, T.D. Anthopoulos, 18.4 % Organic Solar Cells Using a High Ionization Energy Self-Assembled Monolayer as Hole-Extraction Interlayer, ChemSusChem. 14 (2021) 3569–3578. https://doi.org/10.1002/cssc.202100707.

[26] J. Sun, C. Shou, J. Sun, X. Wang, Z. Yang, Y. Chen, J. Wu, W. Yang, H. Long, Z. Ying, X. Yang, J. Sheng, B. Yan, J. Ye, NiOx-Seeded Self-Assembled Monolayers as Highly Hole-Selective Passivating Contacts for Efficient Inverted Perovskite Solar Cells, Solar RRL. 5 (2021). https://doi.org/10.1002/solr.202100663.

[27] M. Ozaki, Y. Ishikura, M.A. Truong, J. Liu, I. Okada, T. Tanabe, S. Sekimoto, T. Ohtsuki, Y. Murata, R. Murdey, A. Wakamiya, Iodine-rich mixed composition perovskites optimised for tin(iv) oxide transport layers: The influence of halide ion ratio, annealing time, and ambient air aging on solar cell performance, Journal of Materials Chemistry A. 7 (2019) 16947–16953. https://doi.org/10.1039/c9ta02142f.

[28] A. Al-Ashouri, A. Magomedov, M. Roß, M. Jošt, M. Talaikis, G. Chistiakova, T. Bertram, J.A. Márquez, E. Köhnen, E. Kasparavičius, S. Levcenco, L. Gil-Escrig, C.J. Hages, R. Schlatmann, B. Rech, T. Malinauskas, T. Unold, C.A. Kaufmann, L. Korte, G. Niaura, V. Getautis, S. Albrecht, Conformal monolayer contacts with lossless interfaces for perovskite single junction and monolithic tandem solar cells, Energy and Environmental Science. 12 (2019) 3356–3369. https://doi.org/10.1039/c9ee02268f.

[29] F. Yang, J. Liu, H.E. Lim, Y. Ishikura, K. Shinokita, Y. Miyauchi, A. Wakamiya, Y. Murata, K. Matsuda, High Bending Durability of Efficient Flexible Perovskite Solar Cells Using Metal Oxide Electron Transport Layer, Journal of Physical Chemistry C. 122 (2018) 17088–17095. https://doi.org/10.1021/acs.jpcc.8b05008.

[30] M. Ozaki, A. Shimazaki, M. Jung, Y. Nakaike, N. Maruyama, S. Yakumaru, A.I. Rafieh, T. Sasamori, N. Tokitoh, P. Ekanayake, Y. Murata, R. Murdey, A. Wakamiya, A Purified,

Solvent-Intercalated Precursor Complex for Wide-Process-Window Fabrication of Efficient Perovskite Solar Cells and Modules, Angewandte Chemie International Edition. 58 (2019) 9389–9393. https://doi.org/10.1002/anie.201902235.

[31] M. Ozaki, Y. Nakaike, A. Shimazaki, M. Jung, N. Maruyama, S. Yakumaru, A.I. Rafieh, P. Ekanayake, T. Saito, Y. Shimakawa, T. Sasamori, Y. Murata, R. Murdey, A. Wakamiya, How to Make Dense and Flat Perovskite Layers for Efficient Solar Cells: Oriented, Crystalline Perovskite Intermediates and Their Thermal Conversion, Bull Chem Soc Jpn. 92 (2019) 1972–1979. https://doi.org/10.1246/bcsj.20190241.

[32] M. Saliba, M. Stolterfoht, C.M. Wolff, D. Neher, A. Abate, Measuring Aging Stability of Perovskite Solar Cells, Joule. 2 (2018) 1019–1024. https://doi.org/10.1016/j.joule.2018.05.005.

[33] K.O. Brinkmann, T. Becker, F. Zimmermann, C. Kreusel, T. Gahlmann, M. Theisen, T. Haeger, S. Olthof, C. Tückmantel, M. Günster, T. Maschwitz, F. Göbelsmann, C. Koch, D. Hertel, P. Caprioglio, F. Peña-Camargo, L. Perdigón-Toro, A. Al-Ashouri, L. Merten, A. Hinderhofer, L. Gomell, S. Zhang, F. Schreiber, S. Albrecht, K. Meerholz, D. Neher, M. Stolterfoht, T. Riedl, Perovskite–organic tandem solar cells with indium oxide interconnect, Nature. 604 (2022) 280–286. https://doi.org/10.1038/s41586-022-04455-0.

[34] H. Chen, S. Teale, B. Chen, Y. Hou, L. Grater, T. Zhu, K. Bertens, S.M. Park, H.R. Atapattu, Y. Gao, M. Wei, A.K. Johnston, Q. Zhou, K. Xu, D. Yu, C. Han, T. Cui, E.H. Jung, C. Zhou, W. Zhou, A.H. Proppe, S. Hoogland, F. Laquai, T. Filleter, K.R. Graham, Z. Ning, E.H. Sargent, Quantum-size-tuned heterostructures enable efficient and stable inverted perovskite solar cells, Nature Photonics. 16 (2022) 352–358. https://doi.org/10.1038/s41566-022-00985-1.

[35] U. Rau, B. Blank, T.C.M. Müller, T. Kirchartz, Efficiency Potential of Photovoltaic Materials and Devices Unveiled by Detailed-Balance Analysis, Physical Review Applied. 7 (2017) 044016. https://doi.org/10.1103/PhysRevApplied.7.044016.

[36] S. Draguta, O. Sharia, S.J. Yoon, M.C. Brennan, Y. v. Morozov, J.M. Manser, P. v. Kamat, W.F. Schneider, M. Kuno, Rationalizing the light-induced phase separation of mixed halide organic-inorganic perovskites, Nature Communications. 8 (2017). https://doi.org/10.1038/s41467-017-00284-2.

[37] W. Mao, C.R. Hall, A.S.R. Chesman, C. Forsyth, Y.B. Cheng, N.W. Duffy, T.A. Smith, U. Bach, Visualizing Phase Segregation in Mixed-Halide Perovskite Single Crystals, Angewandte Chemie - International Edition. 58 (2019) 2893–2898. https://doi.org/10.1002/anie.201810193.

[38] K. Frohna, M. Anaya, S. Macpherson, J. Sung, T.A.S. Doherty, Y.-H. Chiang, A.J. Winchester, K.W.P. Orr, J.E. Parker, P.D. Quinn, K.M. Dani, A. Rao, S.D. Stranks, Nanoscale chemical heterogeneity dominates the optoelectronic response of alloyed perovskite solar cells, Nature Nanotechnology. 17 (2022) 190–196. https://doi.org/10.1038/s41565-021-01019-7.

[39] P. Gratia, G. Grancini, J.N. Audinot, X. Jeanbourquin, E. Mosconi, I. Zimmermann, D. Dowsett, Y. Lee, M. Grätzel, F. de Angelis, K. Sivula, T. Wirtz, M.K. Nazeeruddin, Intrinsic Halide Segregation at Nanometer Scale Determines the High Efficiency of Mixed Cation/Mixed Halide Perovskite Solar Cells, J Am Chem Soc. 138 (2016) 15821–15824. https://doi.org/10.1021/jacs.6b10049.

[40] R.E. Beal, N.Z. Hagström, J. Barrier, A. Gold-Parker, R. Prasanna, K.A. Bush, D. Passarello, L.T. Schelhas, K. Brüning, C.J. Tassone, H.G. Steinrück, M.D. McGehee, M.F. Toney, A.F. Nogueira, Structural Origins of Light-Induced Phase Segregation in Organic-Inorganic Halide Perovskite Photovoltaic Materials, Matter. 2 (2020) 207–219. https://doi.org/10.1016/j.matt.2019.11.001.

[41] T. Elmelund, B. Seger, M. Kuno, P. v. Kamat, How Interplay between Photo and Thermal Activation Dictates Halide Ion Segregation in Mixed Halide Perovskites, ACS Energy Letters. 5 (2020) 56–63. https://doi.org/10.1021/acsenergylett.9b02265.

[42] P. Nandi, Z. Li, Y. Kim, T.K. Ahn, N.-G. Park, H. Shin, Stabilizing Mixed Halide Lead Perovskites against Photoinduced Phase Segregation by A-Site Cation Alloying, ACS Energy Letters. 6 (2021) 837–847. https://doi.org/10.1021/acsenergylett.0c02631.

[43] H. Tsai, R. Asadpour, J.C. Blancon, C.C. Stoumpos, O. Durand, J.W. Strzalka, B. Chen, R. Verduzco, P.M. Ajayan, S. Tretiak, J. Even, M.A. Alam, M.G. Kanatzidis, W. Nie, A.D. Mohite, Light-induced lattice expansion leads to high-efficiency perovskite solar cells, Science (1979). 360 (2018) 67–70. https://doi.org/10.1126/science.aap8671.

[44] A. Ullah, K.H. Park, H.D. Nguyen, Y. Siddique, S.F.A. Shah, H. Tran, S. Park, S.I. Lee, K. Lee, C. Han, K. Kim, S. Ahn, I. Jeong, Y.S. Park, S. Hong, Novel Phenothiazine-Based

Self-Assembled Monolayer as a Hole Selective Contact for Highly Efficient and Stable p-i-n Perovskite Solar Cells, Advanced Energy Materials. 12 (2022) 2103175. https://doi.org/10.1002/aenm.202103175.

[45] F. Fabregat-Santiago, G. Garcia-Belmonte, I. Mora-Seró, J. Bisquert, Characterization of nanostructured hybrid and organic solar cells by impedance spectroscopy, Physical Chemistry Chemical Physics. 13 (2011) 9083. https://doi.org/10.1039/c0cp02249g.

[46] R. Cheng, C. Chung, H. Zhang, F. Liu, W. Wang, Z. Zhou, S. Wang, A.B. Djurišić, S. Feng, Tailoring Triple-Anion Perovskite Material for Indoor Light Harvesting with Restrained Halide Segregation and Record High Efficiency Beyond 36%, Advanced Energy Materials. 9 (2019) 1901980. https://doi.org/10.1002/aenm.201901980.

SUPPORTING INFORMATION FOR

Operational stability, low light performance, and long-lived transients in mixed-halide perovskite solar cells with a monolayer-based hole transport layer

Richard Murdey[*,1], Yasuhisa Ishikura[2], Yuko Matsushige[1], Shuaifeng Hu[1], Jorge Pascual[1], Minh Anh Truong[1], Tomoya Nakamura[1], Atsushi Wakamiya[1]

[1]Institute for Chemical Research, Kyoto University, Gokasho, Uji, Kyoto 611-0011, Japan

[2]Enecoat Technologies, Co. Ltd., Sakosotoyashiki 43-1, Kumiyama, Kuse, Kyoto 613-0031, Japan

*Corresponding author

E-mail address: *murdey@scl.kyoto-u.ac.jp* (R. Murdey)

Table of Contents

Experimental Methods

Materials

Unless otherwise stated, all materials were used as received without further purification. [2-(3,6-dimethoxy-9*H*-carbazol-9-yl)ethyl]phosphonic acid (MeO-2PACz, > 98.0, cesium iodide (CsI, > 99%), methylammonium bromide (MABr, >98.0%), lead(II) bromide ($PbBr_2$, >98.0%), lead(II) iodide (PbI_2, 99.99%, trace metals basis), formamidinium iodide (FAI, > 98.0%), and bathocuproine (BCP) were purchased from Tokyo Chemical Industry Co., Ltd. (TCI).

Poly[bis(4-phenyl)(2,4,6-trimethylphenyl)amine] (PTAA), [tris(2-(1*H*-pyrazol-1-yl)-4-*tert*-butylpyridine)cobalt(III) tris(bis(trifluoromethylsulfonyl)imide)] (FK209) and 4-*tert*-butylpyridine (TBP) were purchased from Sigma-Aldrich Co., Ltd. (Sigma-Aldrich). 2,2′,7,7′-tetrakis(N,N-di-pmethoxyphenylamino)-9,9′-spirobifluorene (spiro-OMeTAD) was purchased from Merck Co., Ltd. Lithium bis(trifluoromethylsulfonyl)imide (LiTFSI) was purchased from Wako Pure Chemical Industries Co., Ltd. Fullerene C_{60} (sublimed, 99.99%) was purchased from ATR Company. Fullerene C_{60} (sublimed, 99.99%) was purchased from ATR Company. Dehydrated dimethyl sulfoxide (DMSO, super dehydrated) was purchased from FUJIFILM Wako Pure Chemical Co., Ltd. Dimethylformamide (DMF), toluene, and chlorobenzene solvents were purchased from Kanto Chemical. Co., Inc. Before use, the solvents were degassed by Ar gas bubbling for 1 h and further dried over molecular sieves (3 Å) in an Ar-filled glove box (H_2O, O_2 < 0.1 ppm).

Substrate and precursor solution

Glass/ITO substrates (10 Ω sq^{-1}) were etched with zinc powder and HCl (6 M in de-ionized water), and consecutively cleaned with 15 min ultrasonic bath in water, acetone, detergent solution (Semico Clean 56, Furuuchi chemical), water, and isopropanol. The substrates were dried with an air gun, and finally plasma treatment. The substrates were transferred to an inert gas-filled glove box for further processing.

The precursor solutions of $Cs_{0.05}FA_{0.80}MA_{0.15}PbI_{2.75}Br_{0.25}$ and $Cs_{0.05}FA_{0.80}MA_{0.15}PbI_2Br$ were prepared from stoichiometric amounts of CsI, MABr, $PbBr_2$, PbI_2, and FAI dissolved in a mixture of 3:1 DMF and DMSO. After stirring at 40 °C for 30 min, the solution was filtered with a 0.45 μm PTFE filter. The concentration of Pb was 1.05 mol L^{-1}.

p-i-n device fabrication (MeO-2PACz, PTAA)

The hole transporting monolayer MeO-2PACz (1 mmol L^{-1} in anhydrous ethanol) was deposited on plasma-treated ITO substrates by using spin-coating (3000 rpm for 30 s, 5 s

acceleration), followed by heating on a hot plate at 100 °C for 10 min. For the PTAA devices, the hole transporting material PTAA (2 mg mL^{-1} in anhydrous toluene) was deposited using spin-coating (4000 rpm for 30 s, 5 s acceleration), followed by heating on a hot plate at 100 °C for 10 min. 190 µL of the perovskite precursor solution was placed on an ITO/MeO-2PACz substrate and spread by spin-coating (slope 1 s, 1000 rpm 10 s, slope 5 s, 3000 rpm 20 s, slope 1 s) to make a thin film. 300 µL of chlorobenzene antisolvent was dripped over the rotating substrate 3 s before the end of the spinning at 3000 rpm. The films were then annealed on a hot plate at 150 °C for 10 min.

The samples were transferred under an inert atmosphere to a vacuum deposition chamber, where 20 nm of C_{60} (deposition rate 0.05 nm s^{-1}) and 8 nm of BCP (deposition rate 0.01 nm s^{-1}) were deposited by thermal evaporation.

The top electrode was prepared by depositing 100 nm of silver (deposition rate 0.005 nm s^{-1}) through a shadow mask.

n-i-p device fabrication (Spiro-OMeTAD)

The SnO_2 layer was prepared by spin-coating a colloidal dispersion (15% in H_2O, 3.0 mL) diluted with deionized water (3.0 mL) on the glass-ITO substrates (slope 2 s, 2000 rpm 30 s, slope 2 s) followed by annealing at 150 °C for 30 min. A plasma treatment was performed after cooling the substrate to room temperature, before transferring the samples to an inert gas-filled glove box.

190 µL of the perovskite precursor solution was placed on an ITO/SnO_2 substrate and spread by spin-coating (slope 1 s, 1000 rpm 10 s, slope 5 s, 3000 rpm 20 s, slope 1 s) to make a thin film. 300 µL of chlorobenzene was dripped over the rotating substrate at 3 s before the end of the spinning at 3000 rpm. The films were then annealed on a hot plate at 150 °C for 10 min.

Hole-transporting material (Spiro-OMeTAD 0.06 M) was mixed with an oxidizing agent [tris(2-(1*H*-pyrazol-1-yl)-4-*tert*-butylpyridine)cobalt(III) tris(bis(trifluoromethylsulfonyl)imide)] (FK209, 0.03 equiv) into a solution of chlorobenzene (1 mL), 4-*tert*-butylpyridine (TBP, 3.3 equiv), and lithium bis(trifluoromethylsulfonyl)imide (LiTFSI, 0.54 equiv). After stirring at 70 °C for 30 min, the suspension was filtered with a 0.45 µm PTFE filter to remove insoluble Co(II) complexes. 90 µL of the solution was spin-coated on top of the perovskite layer (slope 4 s, 4000 rpm, 30 s, slope 4 s), followed by annealing at 70 °C for 30 min.

Gold electrodes (80 nm) were thermally deposited on the top face of the devices using a shadow mask.

The measurement environment

All devices were briefly exposed to air to remove material covering the ITO electrode, and apply solder to the exposed ITO to lower the contact resistance. From this point onwards all devices were stored in the dark in a nitrogen-filled glovebox. A single substrate was transferred to a small, inert-gas-filled chamber (ALS technologies, KC-94) for measurement. The cell under test, which had an active area delimited by a 0.1 cm^2 metal mask, could be exposed to light through a quartz window. The measurement environment is not temperature controlled, and the sample temperature under AM1.5G rises to about 30 °C above ambient. At no point after fabrication were the devices exposed to air.

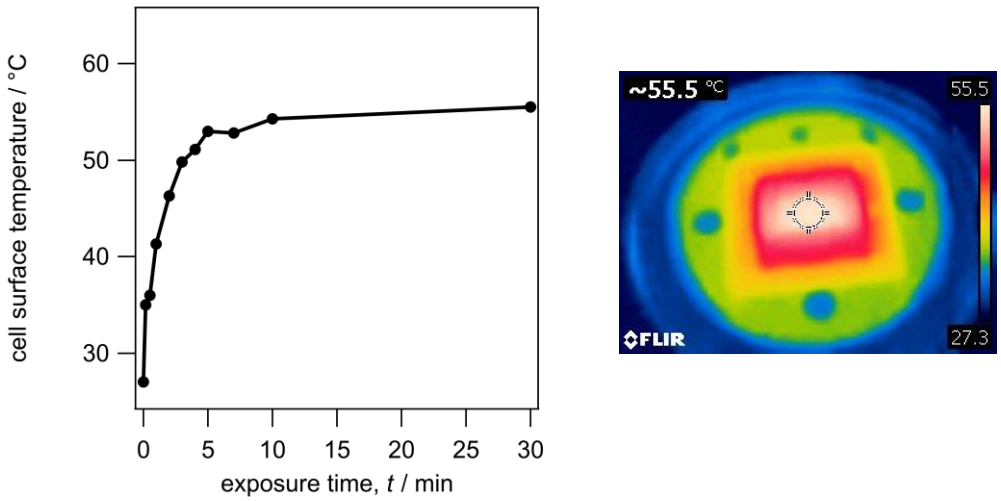

Estimation of the cell temperature under AM1.5G using an infrared camera (FLIR C2).

Scanning electron microscopy

Scanning electron microscopy (SEM) was performed with a Hitachi S8010 ultra-high-resolution scanning electron microscope (Hitachi High-Tech Corporation).

Light sources

AM1.5G and attenuated AM1.5G light were generated with a Bunkoukeiki SMO-250PV solar simulator using a 150 W Xe lamp. The light intensity was calibrated using a Bunkoukeiki BS-520BK reference silicon photodiode with an IR-cut filter. Attenuation over a wide range of intensity was enabled by using various neutral density filters (100, 40, 20, 10, 5, and 1% transmittance) in combination with the variable aperture built into the solar simulator. Transmission through the neutral density filters is wavelength-dependent, hence the true attenuation of each filter depends on the spectral sensitivity of the device. The filters were therefore calibrated using a perovskite solar cell with the same bandgap as the sample. Calibration

factors, given in the table below, are determined by cross-correlating attenuation data at three different aperture settings.

Calibrated transmission of the neutral density filters for the $Cs_{0.05}FA_{0.80}MA_{0.15}PbI_{2.75}Br_{0.25}$ "low-Br" and $Cs_{0.05}FA_{0.80}MA_{0.15}PbI_2Br$ "high-Br" perovskite materials.

Nominal Value	Transmittance (%) Calibrated with the Low-Br/MeO-2PACz device	Calibrated with the High-Br/MeO-2PACz device
100 (No Filter)	100 (Reference)	100 (Reference)
40	44.1±0.5	43.6±0.1
20	22.3±0.2	21.9±0.1
10	11.6±0.1	11.3±0.1
5	6.33±0.10	6.03±0.05
1	1.27±0.03	1.17±0.01

Ambient light was simulated with a 50 W white LED (OptoSupply OSW4XAHCE1E) powered by an adjustable power supply set to 25 V and 12 mA (0.31 W) producing an irradiance of 250 μW/cm^2 (835 lx) at the sample. The source-to-sample distance was about 15 cm. No temperature rise was noted, and no focusing optics were used. Ambient light measurements were performed in a light-tight environment. The spectral irradiance between 380 and 780 nm was determined with a Sekonic Spectromaster C-7000 handheld spectrometer.

J–V and MPPT measurements

J–V curves were obtained using a Keithley 2450 sourcemeter. Forward and reverse scans were measured between −0.1 and 1.2 V at a scan rate of 50 mV s^{-1}. The Keithley 2450 was also used to perform the maximum power point tracking (MPPT) measurements, using a step-and-check algorithm written in Labview.

J–V curves were normally measured following 300 s operation under MPPT conditions. The final output power at the end of the 300 s MPPT sequence was taken as the device PCE, while J_{sc}, V_{oc}, and FF were calculated as the value from the forward and reverse *J–V* curves. We find this methodology generally provides a more reliable assessment of the electrical characteristics than instantaneous *J–V* curves recorded immediately after the device is exposed to the light source. An exception was made when measuring the light intensity dependence using attenuated AM1.5G. The properties of the perovskite devices often varied slightly depending on their measurement history. To minimize this effect while taking measurements at widely different light intensities, exposure times were kept low by only measuring *J–V* scans. During the 100 h MPPT stability test,

the MPPT algorithm is briefly halted every 20 minutes while forward and reverse *J*–*V* curves are recorded. This allows us to monitor the change in J_{sc}, V_{oc}, and FF over the 100-h interval as well as the PCE.

EQE spectra

EQE spectra were recorded between 300 and 1100 nm with light from a Bunkoukeiki SM-250 Monolight System featuring a 150 W Xe lamp and M25 monochromator. The output was calibrated with a Bunkoukeiki S1337-1010BQ silicon photodiode. Device currents were measured with a Keithley 2450 sourcemeter.

X-ray diffraction measurements

XRD measurements were performed with a Rigaku SmartLab.

Impedance measurements

A Keysight E4990A impedance analyzer was used to record the complex impedance spectra. The oscillation amplitude was 30 mV, and the frequency is scanned from 200 Hz to 20 MHz. The applied forward DC bias was stepped from 0 to 1.2 V, in 0.1 V steps, and a frequency scan recorded at each step. Impedance measurements were taken under AM1.5G following 300 s operation under MPPT.

Shockley–Queisser Calculations

The principle of detailed balance is used to derive the theoretical maximum cell output as a function of the absorber energy gap and the spectral intensity of the light source. Known as the radiative, or Shockley–Queisser limit (SQ limit), the results are typically calculated for the AM1.5G solar spectrum. The narrow bandgap of the low-Br material is more favorable for operation under AM1.5G since more light from the wideband solar spectrum is absorbed., while the wide bandgap of the high-Br perovskite is better suited for operation under the white LED due to the higher cell voltage.

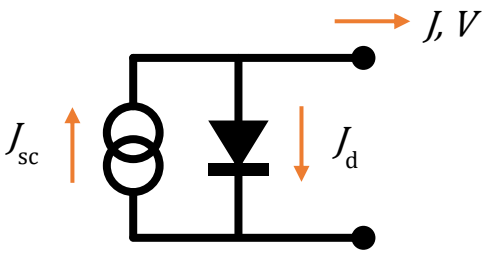

$$J_{\mathrm{d}} = J_s\left(e^{\frac{V}{nV_T}} - 1\right)$$

$$J = J_{sc} - J_s\left(e^{\frac{V}{nV_{\mathrm{T}}}} - 1\right)$$

The equivalence circuit for a simple solar cell neglecting any resistive or capacitive elements is shown above. In this example, the photogenerated current – shown as a constant current source – is equal to the short circuit current, J_{sc}. The diode current, J_d, is defined by the Shockley diode equation, given above, which depends on the saturation current, J_s. In these calculations, the ideality factor, n, is unity. The thermal voltage, $V_T = q/k_BT$, is calculated for T = 298 K. k_B is the Boltzmann constant. In the method given by W. Shockley and H. J. Queisser (*J. Appl. Phys.* **1961**, *32*, 510–519.) the *J*–*V* relationships are determined from the maximum obtainable values for J_{sc} and J_s, which are in turn estimated from the absorber bandgap after making several simplifying assumptions: Nonradiative recombination is neglected, and the EQE is approximated by a Heaviside step function transitioning at the absorber bandgap energy E_g, i.e. $H(x–E_g)$. This leads to,

$$J_{sc}^{SQ} = q \int_{E_g}^{\infty} \phi_{AM1.5G}(E)\ \mathrm{d}E$$

$$J_s^{SQ} = q \int_{E_g}^{\infty} \phi_{BB}(E)\ \mathrm{d}E \quad .$$

According to the principle of detailed balance, the saturation current, J_s^{SQ}, can be calculated using the blackbody spectral irradiance,

$$\phi_{BB}(E) = \frac{2\pi E^2}{h^3 c^2} \frac{1}{\exp\left(\frac{E}{k_B T}\right) - 1} \quad .$$

The device efficiency determined from the *J*–*V* curves calculated under these assumptions is known as the Shockley–Queisser (SQ) limit. Normally the short circuit current is determined using $\phi_{AM1.5G}$, the reference spectral irradiance of sunlight, but J_{sc}^{SQ} may be readily determined for any arbitrary light source and intensity by substituting a new irradiance function, such as the one for a white LED shown in **Fig. S6**.

Supplementary Figures

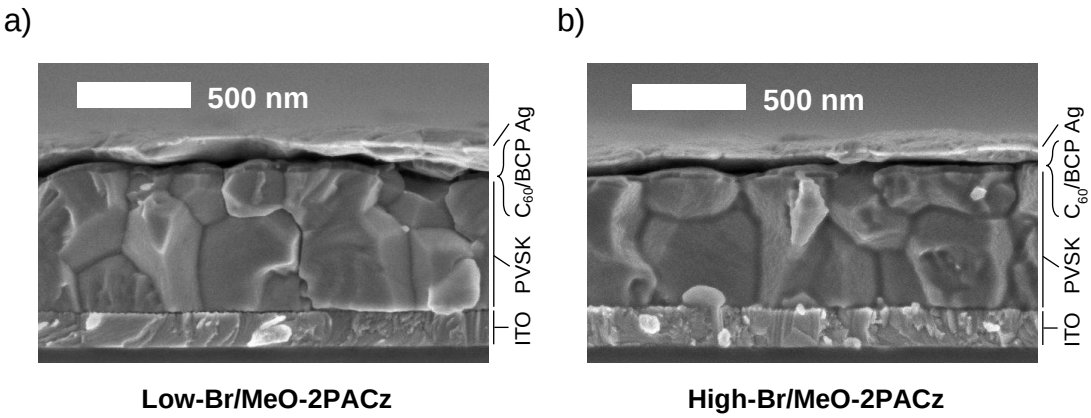

Fig. S1. Cross-sectional SEM images of the p-i-n perovskite solar cells with MeO-2PACz monolayer HTL, fabricated with (a) low-Br perovskite composition and (b) high-Br perovskite composition. The thickness of the perovskite layers is about 600 nm, and the thickness of the bottom ITO layer is 150 nm. The MeO-2PACz monolayer is not resolved. The C_{60} and BCP ETL materials form a 30 nm crust on the top surface of the perovskite, while the Ag electrodes are seen to be partially delaminated. Delamination most likely occurred when the device was cleaved in preparation for the SEM measurements.

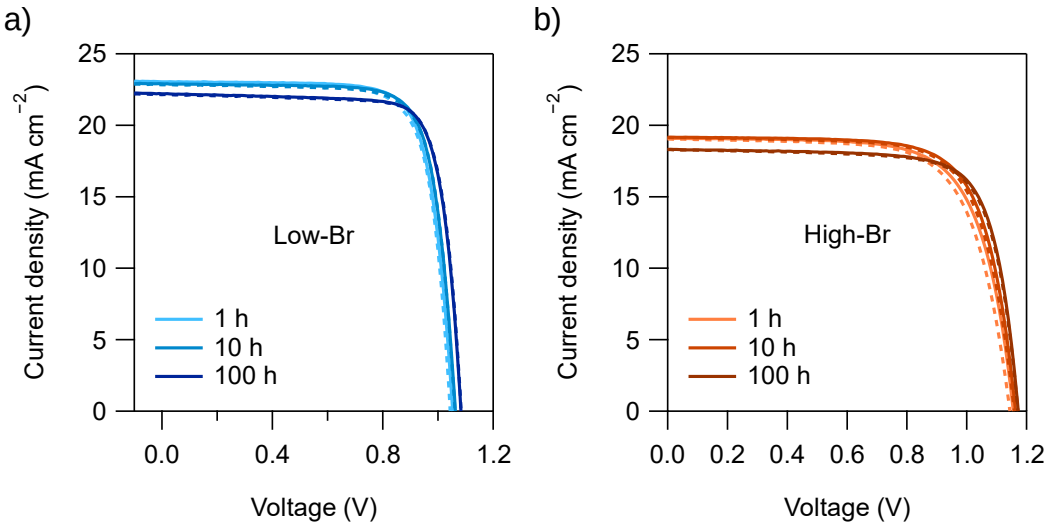

Fig. S2. *J–V* curves recorded after 1, 10, and 100 h MPPT under AM1.5G for the (a) narrow bandgap and (b) wide bandgap devices. (Solid lines: forward scans, dashed lines: reverse scans.)

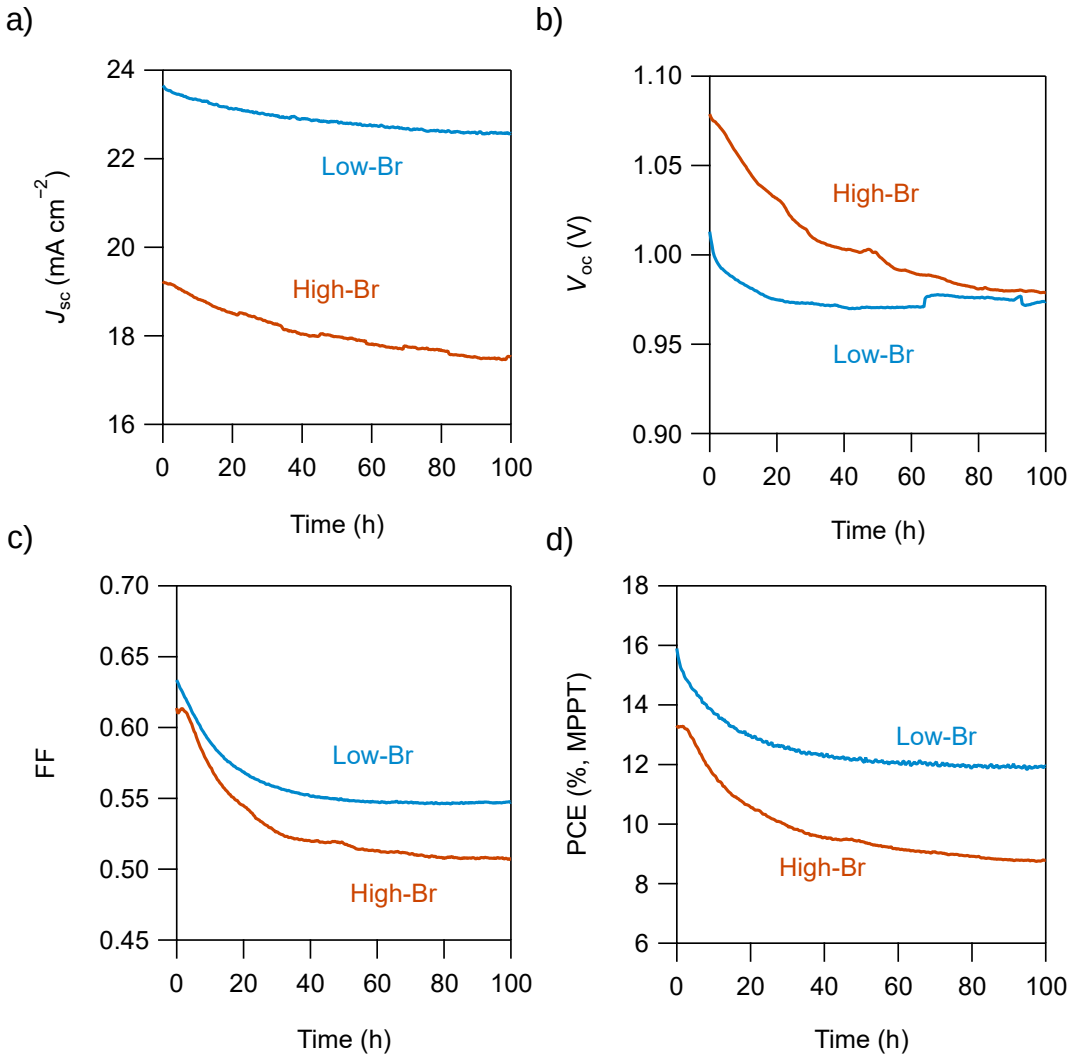

Fig. S3. Electrical performance of n-i-p solar cells (ITO/SnO_2/perovskite/Spiro-OMeTAD/Au) recorded during 100 h MPPT. (a) J_{sc}, (b) V_{oc}, (c) FF, and (d) PCE. The PCE values are determined directly from the MPPT data. The other parameters are derived from *J*–*V* curves recorded at 20-minute intervals.

a)

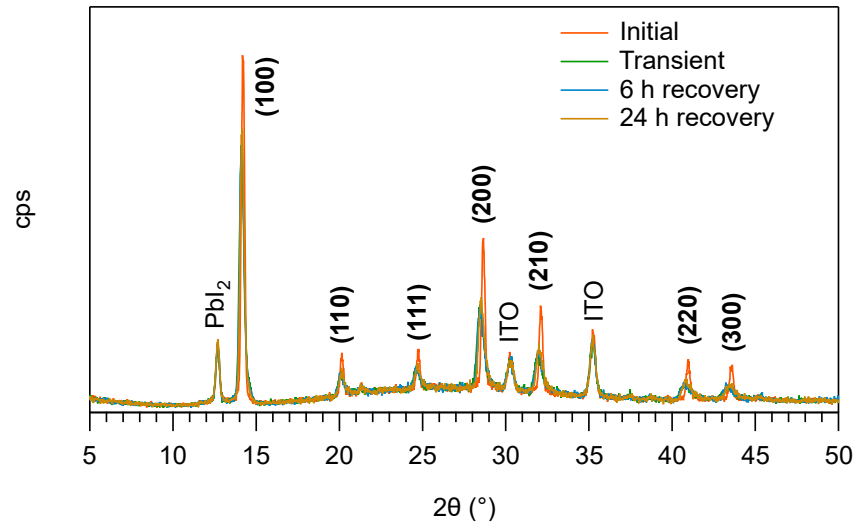

b)

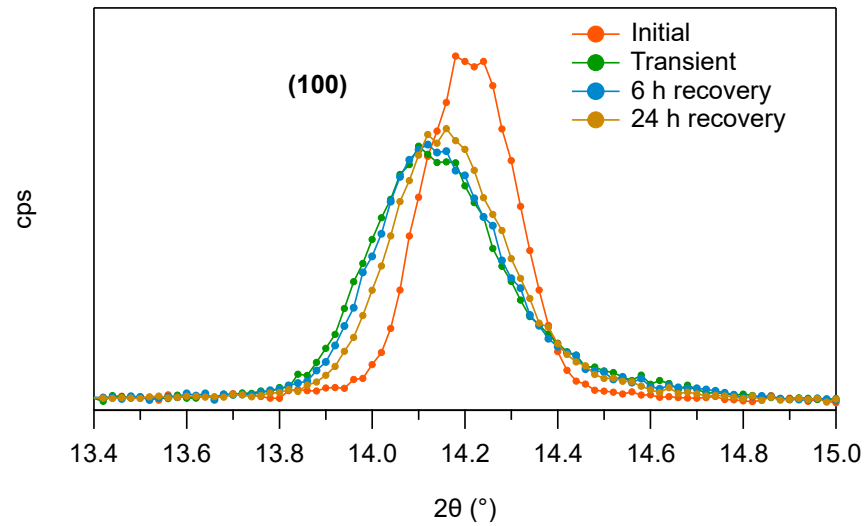

Fig. S4. X-ray diffraction patterns for the high-Br perovskite film on ITO/MeO-2PACz before (Initial) and shortly after 100 h exposure to AM1.5G (Transient), as well as after 6 h and 24 h recovery in the dark.

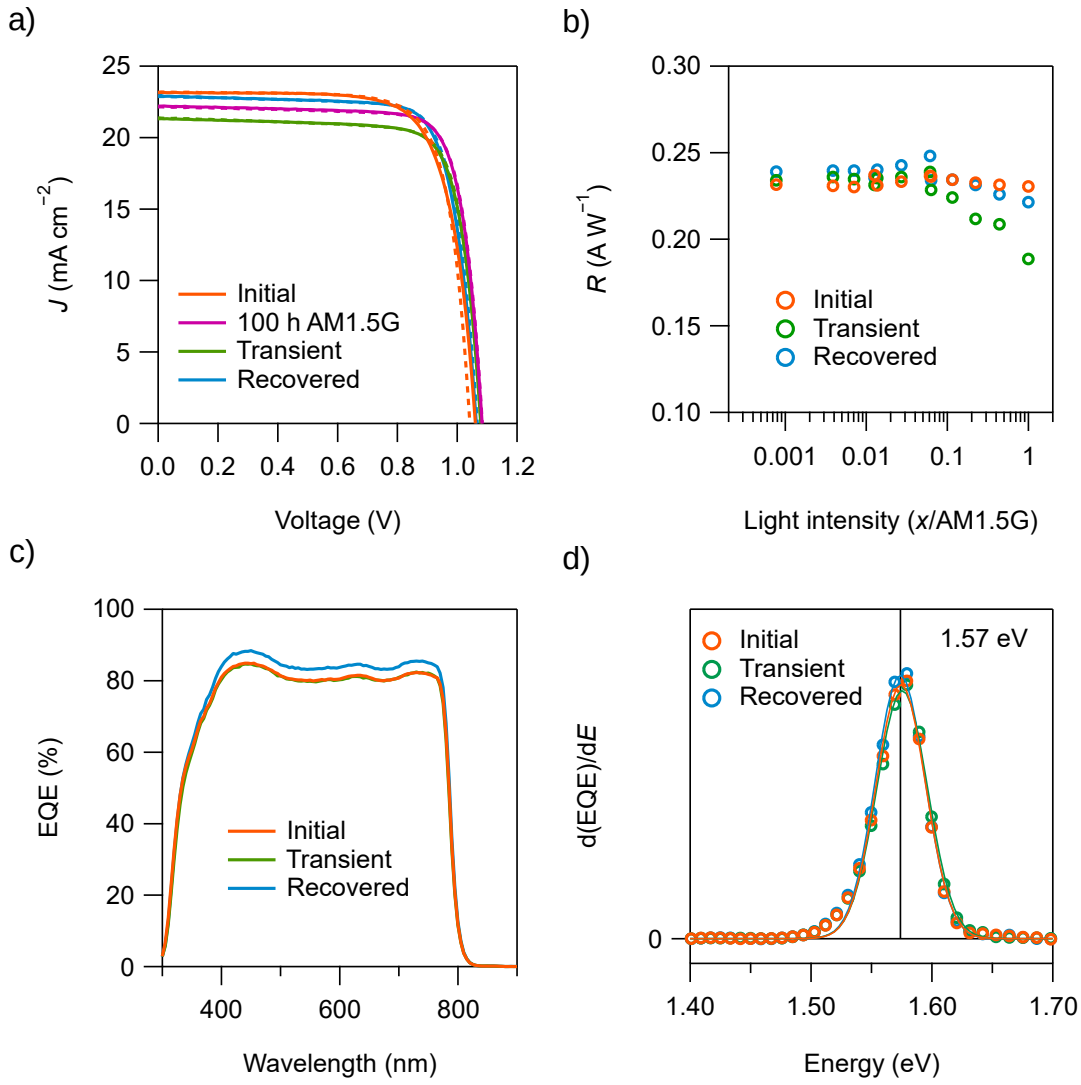

Fig. S5. Properties of the low-Br device before (Initial) and after the 100 h MPPT test (100 h), in the hours following 100 h MPPT (Transient), and after 500 h, by which point the transient effects have subsided (Recovered). (a) Forward (solid line) and reverse (dashed line) *J*–*V* curves under AM1.5G show the significant loss of J_{sc} in the hours following 100 h MPPT. (b) Corresponding loss of device responsivity as a function of light intensity. (c) EQE spectra. (d) The differential of the EQE signal around the onset region. Gaussian peak fits of the experimental data are indicated by the solid lines.

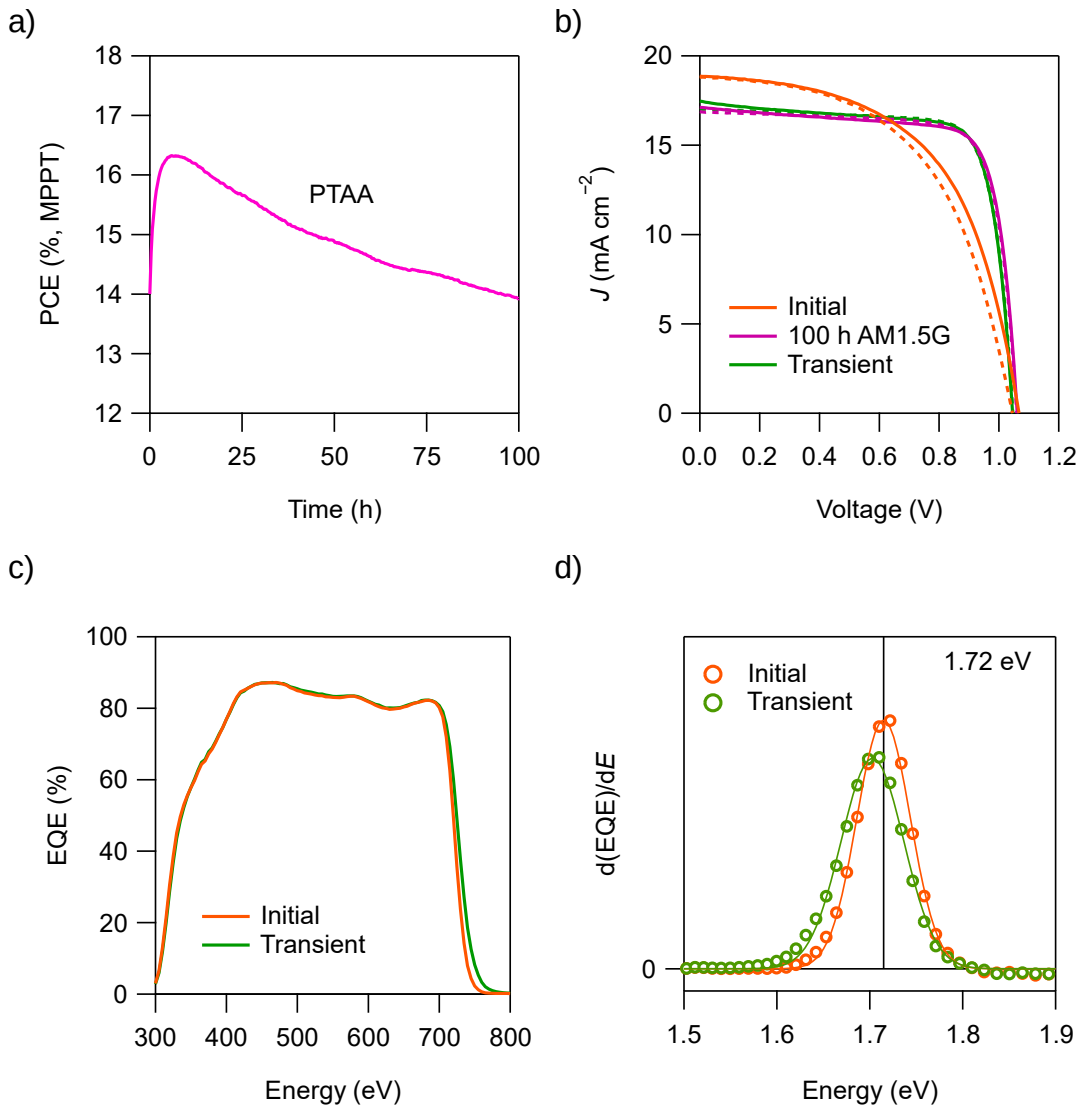

Fig. S6. Characteristics of a p-i-n device fabricated with a PTAA hole transport layer instead of the MeO-2PACz monolayer. The absorber was high-Br perovskite. (a) 100 MPPT stability test under AM1.5G. (b) *J*–*V* curves under AM1.5G. (c) EQE spectra. (d) The differential of the EQE signal around the onset region. Gaussian peak fits of the experimental data are indicated by the solid lines.

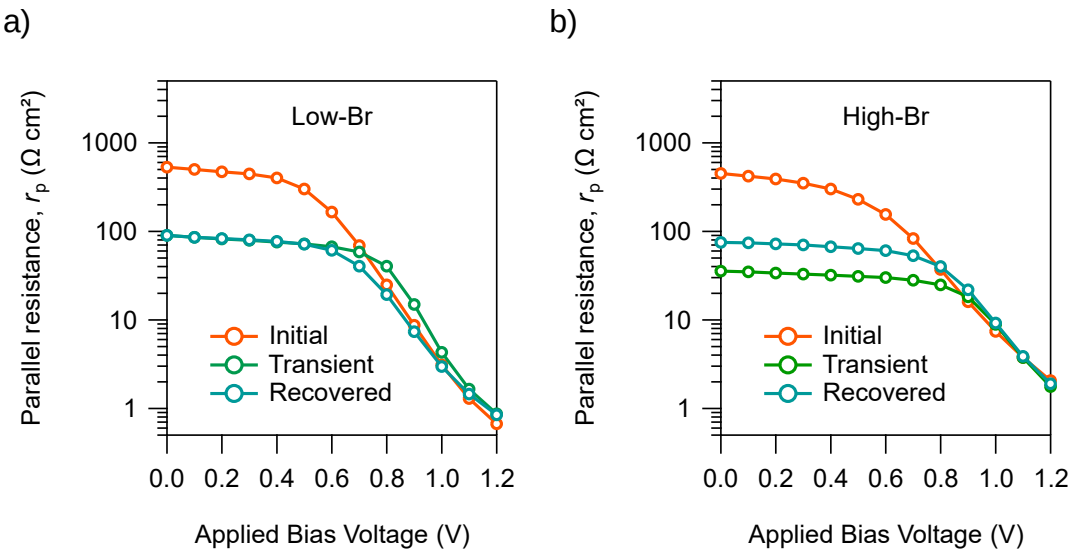

Fig. S7. Evolution of the parallel resistance, r_p, of the test cells as a function of applied bias voltage. Results for the devices before and the 100 h MPPT test (Initial), and in the hours following the end of the MPPT test (Transient), and after the transient effects subside (Recovered) shown for (a) low-Br and (b) high-Br devices. r_p is determined from the complex impedance spectra measured under AM1.5G (data and model fits are given in Appendix A).

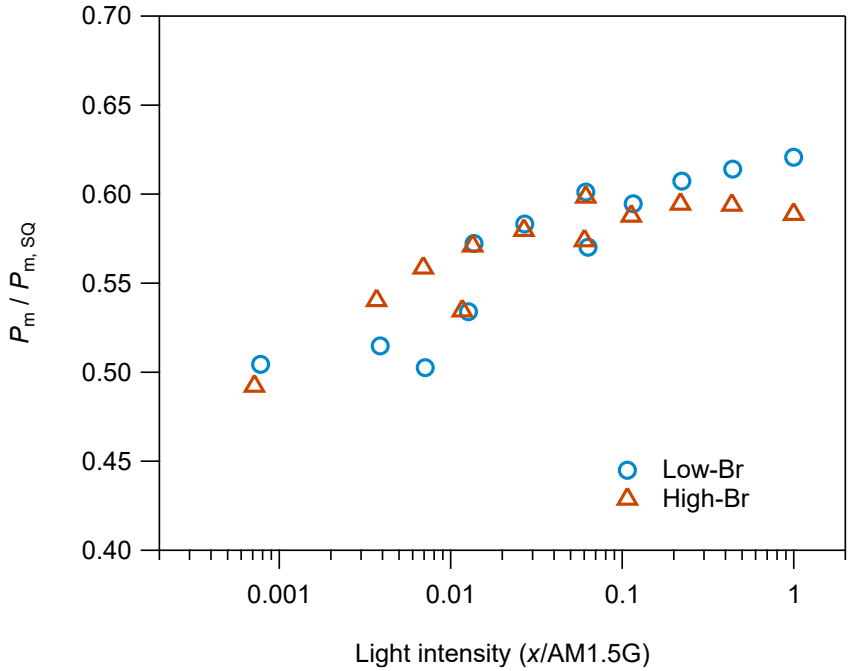

Fig. S8. A plot showing the ratio of the measured maximum output power (determined from the average P_m of the forward and reverse J–V scans) and the Shockley–Queisser limit ($P_{m, SQ}$) for the low-Br and high-Br devices as a function of light intensity. Attenuated AM1.5G illumination was used for these measurements.

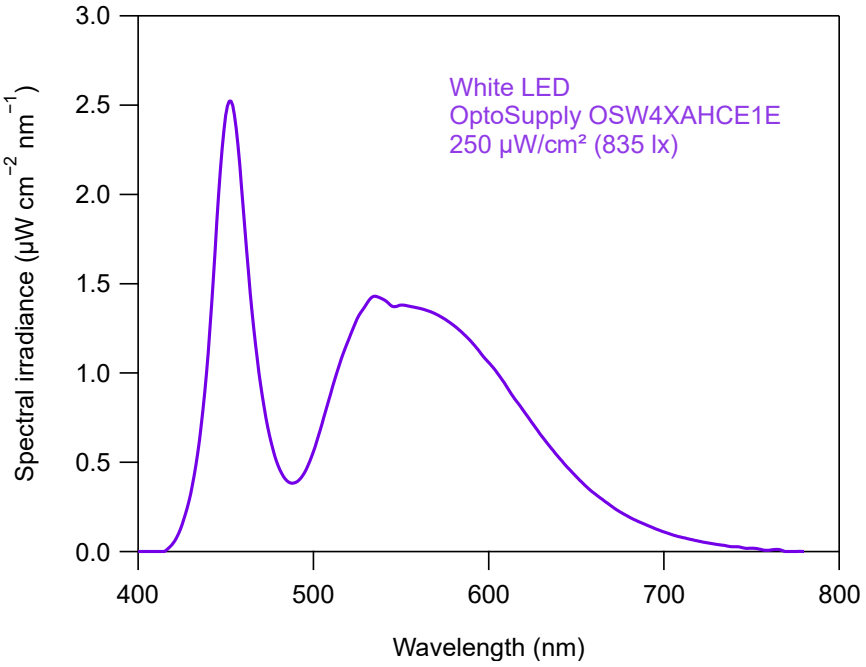

Fig. S9. Spectral intensity of the white LED (OptoSupply OSW4XAHCE1E) that was used to simulate ambient indoor lighting. The irradiance of 250 µW cm^{-2} translates to an illuminance of 835 lx, a typical brightness for a well-lit work environment. The spectrum was recorded with a Sekonic C-7000 color meter.

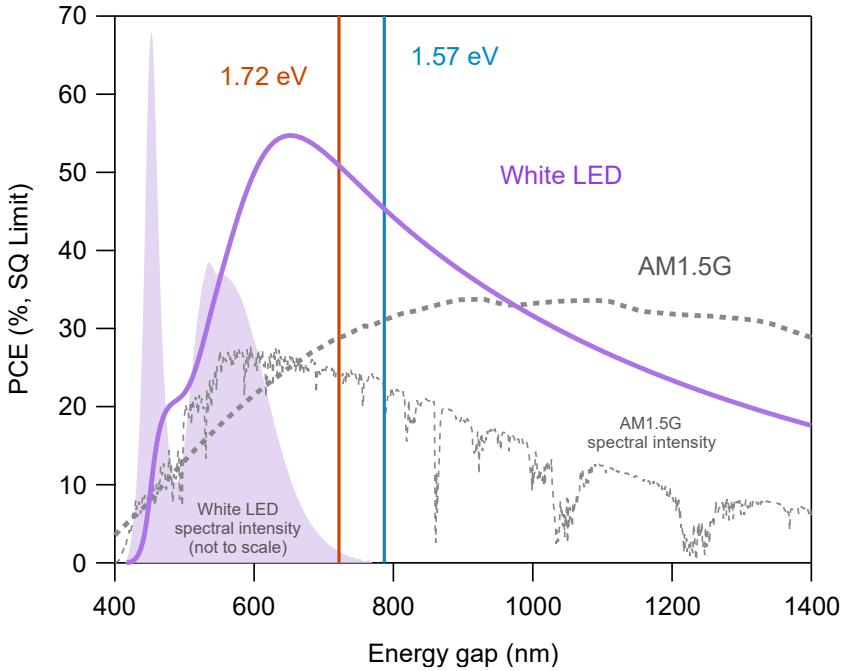

Fig. S10. Detailed balance calculations comparing the theoretical PCE under solar radiation (ASTM G173-03, AM1.5G, 100 mW cm^{-2}) and the low-intensity white LED (irradiance 250 $\mu W/cm^2$) used in this work for the ambient light tests. Very high efficiencies are theoretically possible with the LED due to the narrow bandwidth of the emitted light.

Appendix A: Complex Impedance Spectra

Impedance measurements were taken with a Keysight model E4990A impedance analyzer. The frequency range was scanned from 200 Hz and 20 MHz while the applied bias was increased stepwise from 0 to 1.2 V. The parallel resistance, r_p, is obtained from the model fits indicated by the grey solid line as the diameter of the semicircular feature. Samples were measured under AM1.5G, under an inert atmosphere.

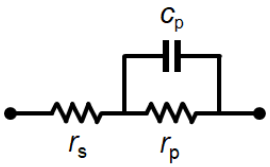

The model circuit for fitting the impedance data.

In the model circuit, the parallel resistance, also called the recombination resistance, derives from the parallel conductance of the diode and shunt resistance elements in the standard solar cell equivalent circuit. The formal relation is $-(dJ/dV) = r_p + r_s$, where r_s is the series resistance of the device and J is the calculated current of the equivalent circuit. r_p will converge to the shunt resistance of the cell at low bias voltages and decrease exponentially at higher voltages due to conduction through the diode element. The current at high bias voltage is eventually limited by the series resistance of the diode element.

Data shown for the following devices and conditions:

Low-Br (Initial)

Low-Br (Transient)

Low-Br (Recovered)

High-Br (Initial)

High-Br (Transient)

High-Br (Recovered)

Low-Br (Initial)

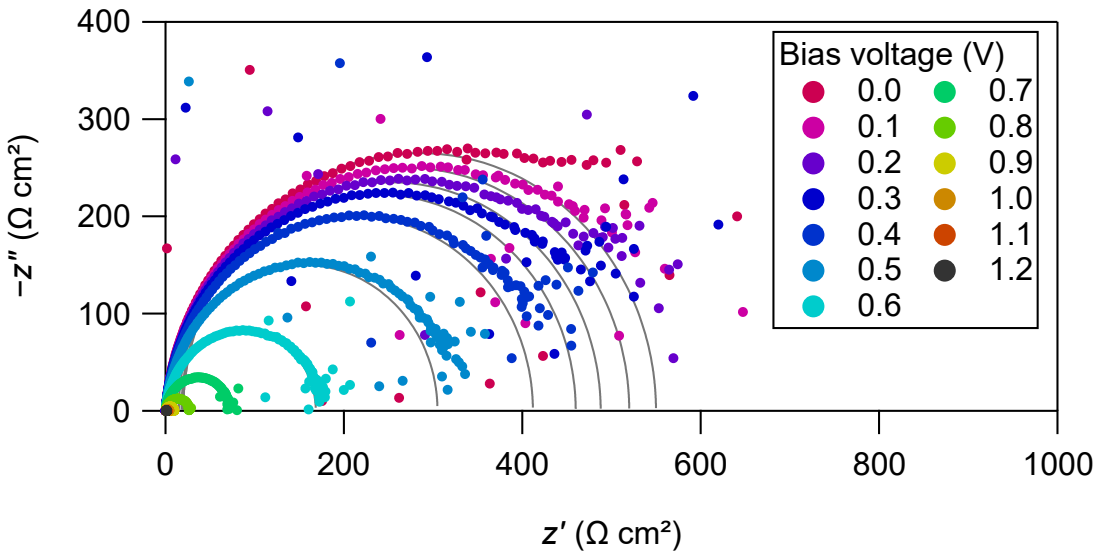

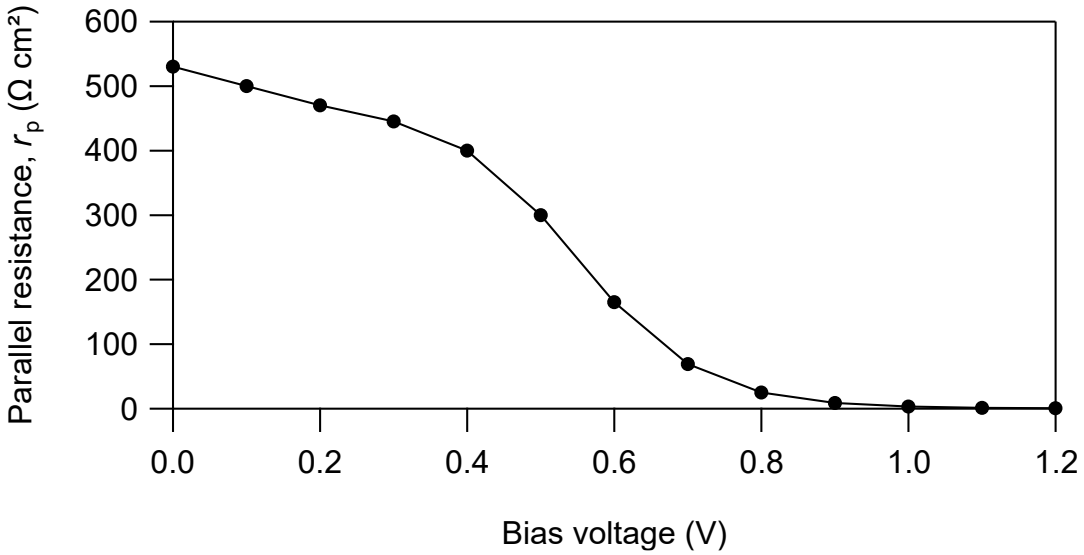

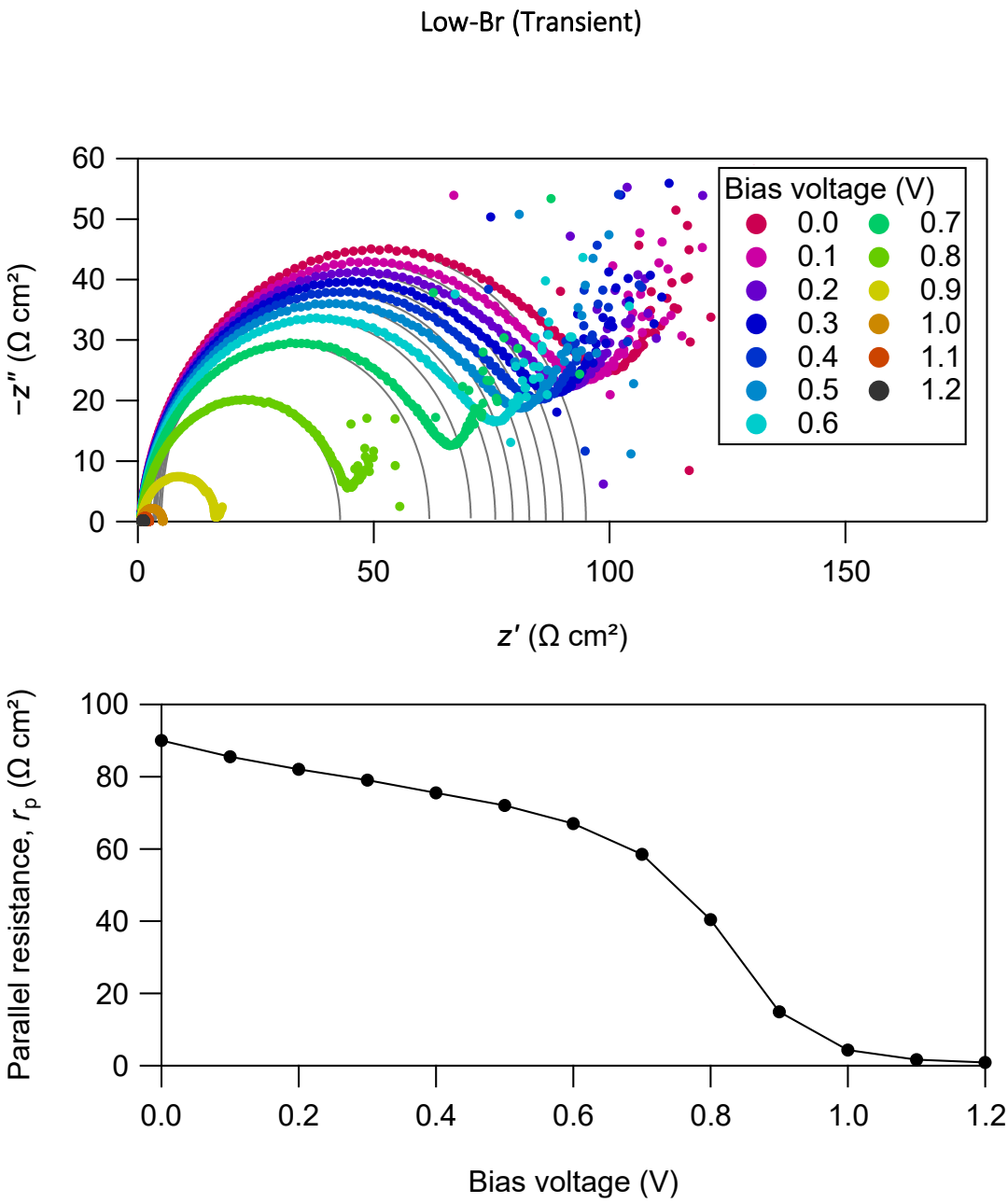
Low-Br (Transient)
Bias voltage (V)
0.0
0.1
0.2
0.3
0.4
0.5
0.6
0.7
0.8
0.9
1.0
1.1
1.2
−z″ (Ω cm²)
z′ (Ω cm²)
Parallel resistance, r_p (Ω cm²)
Bias voltage (V)

Low-Br (Recovered)

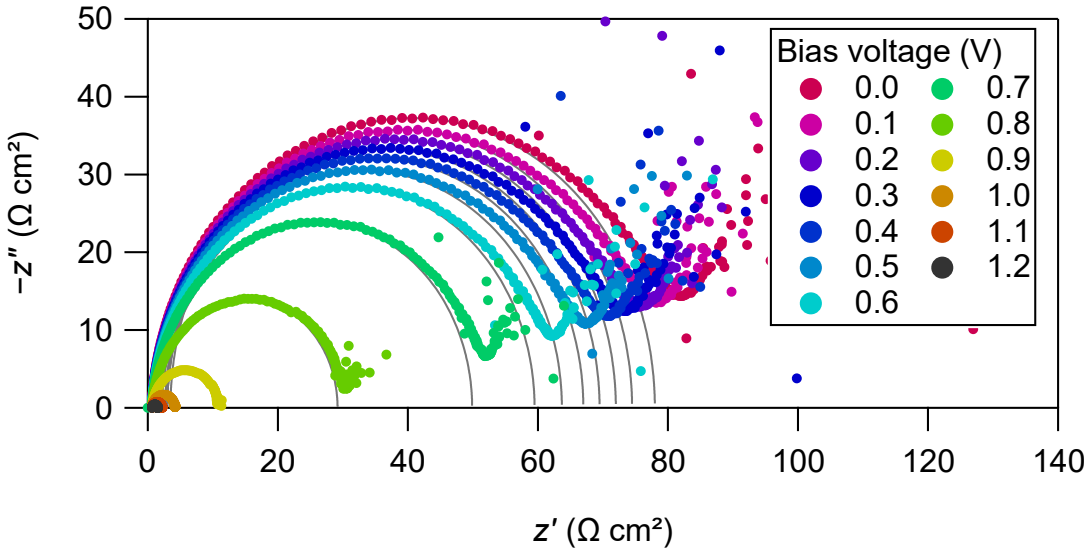

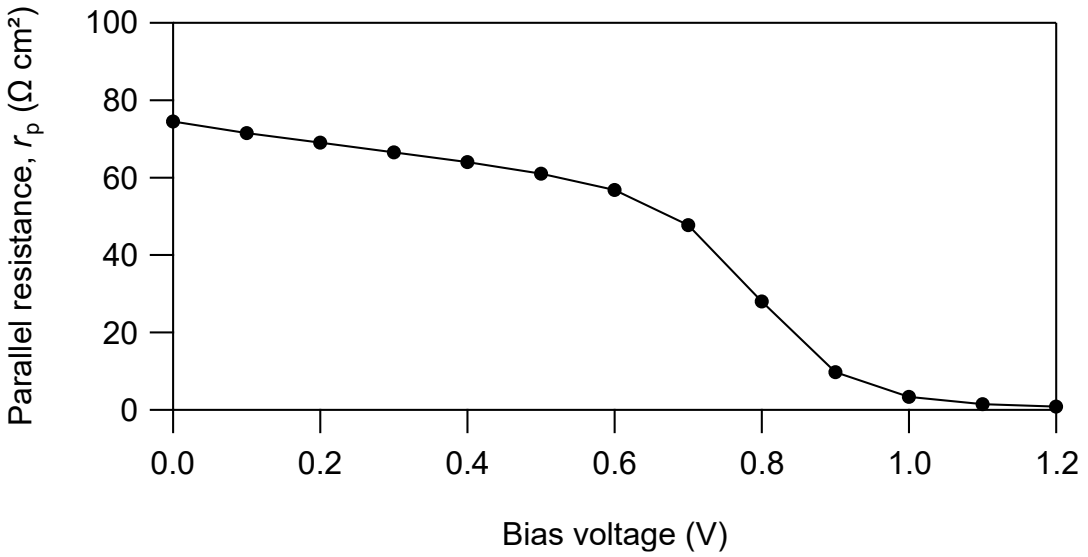

High-Br (Initial)

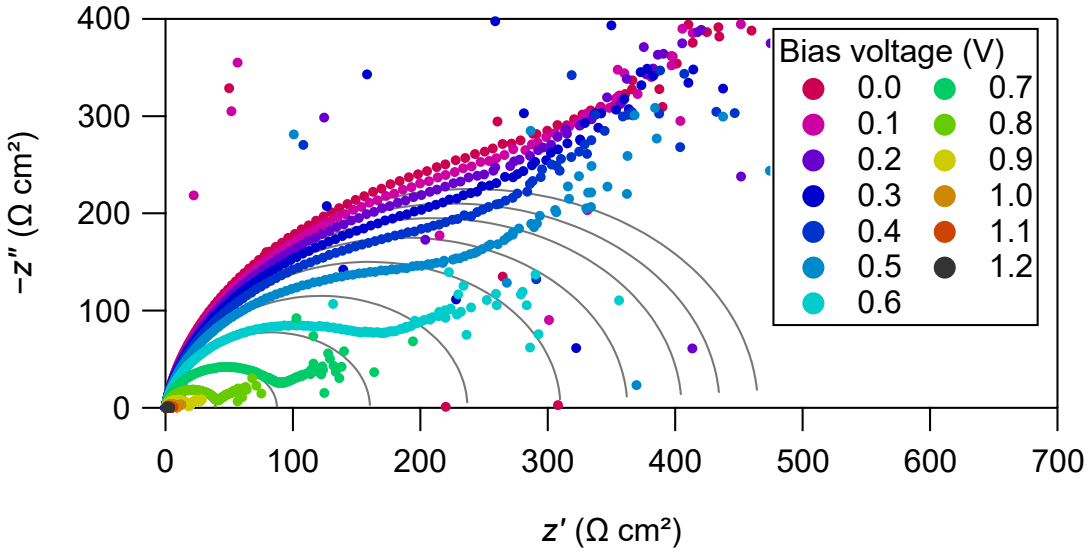

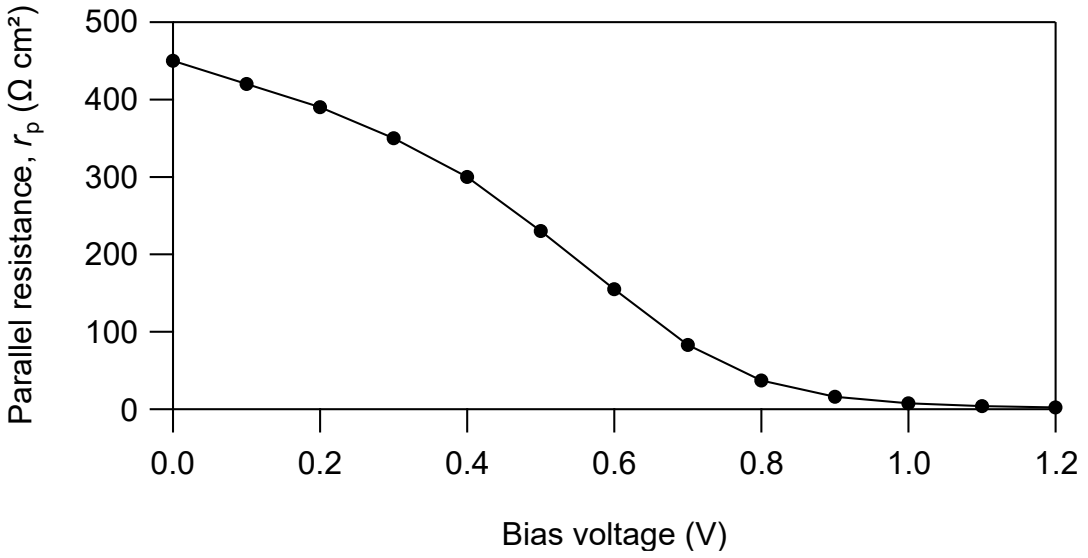

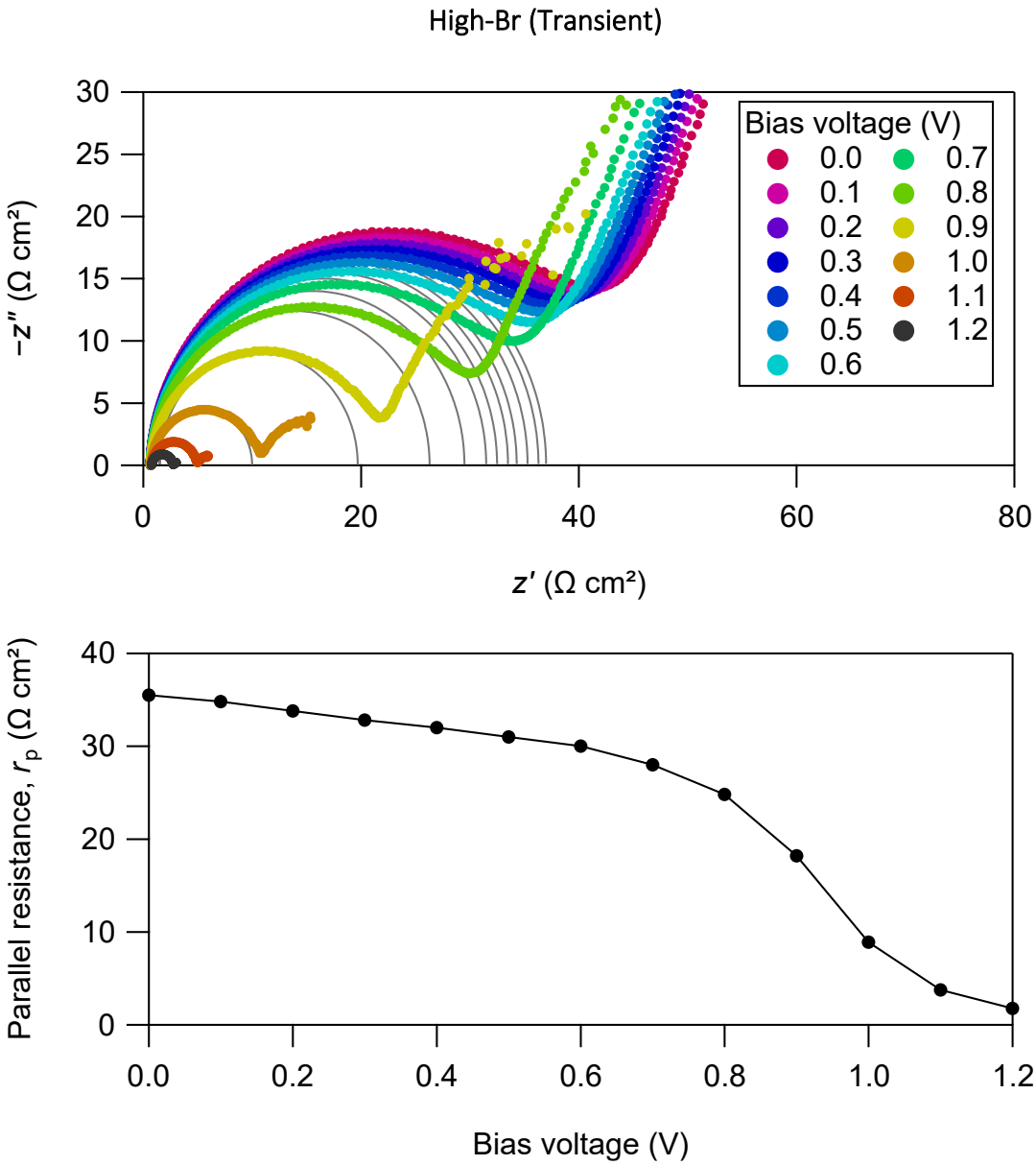
High-Br (Transient)
Bias voltage (V)
0.0
0.1
0.2
0.3
0.4
0.5
0.6
0.7
0.8
0.9
1.0
1.1
1.2
−z″ (Ω cm²)
z′ (Ω cm²)
Parallel resistance, r_p (Ω cm²)
Bias voltage (V)

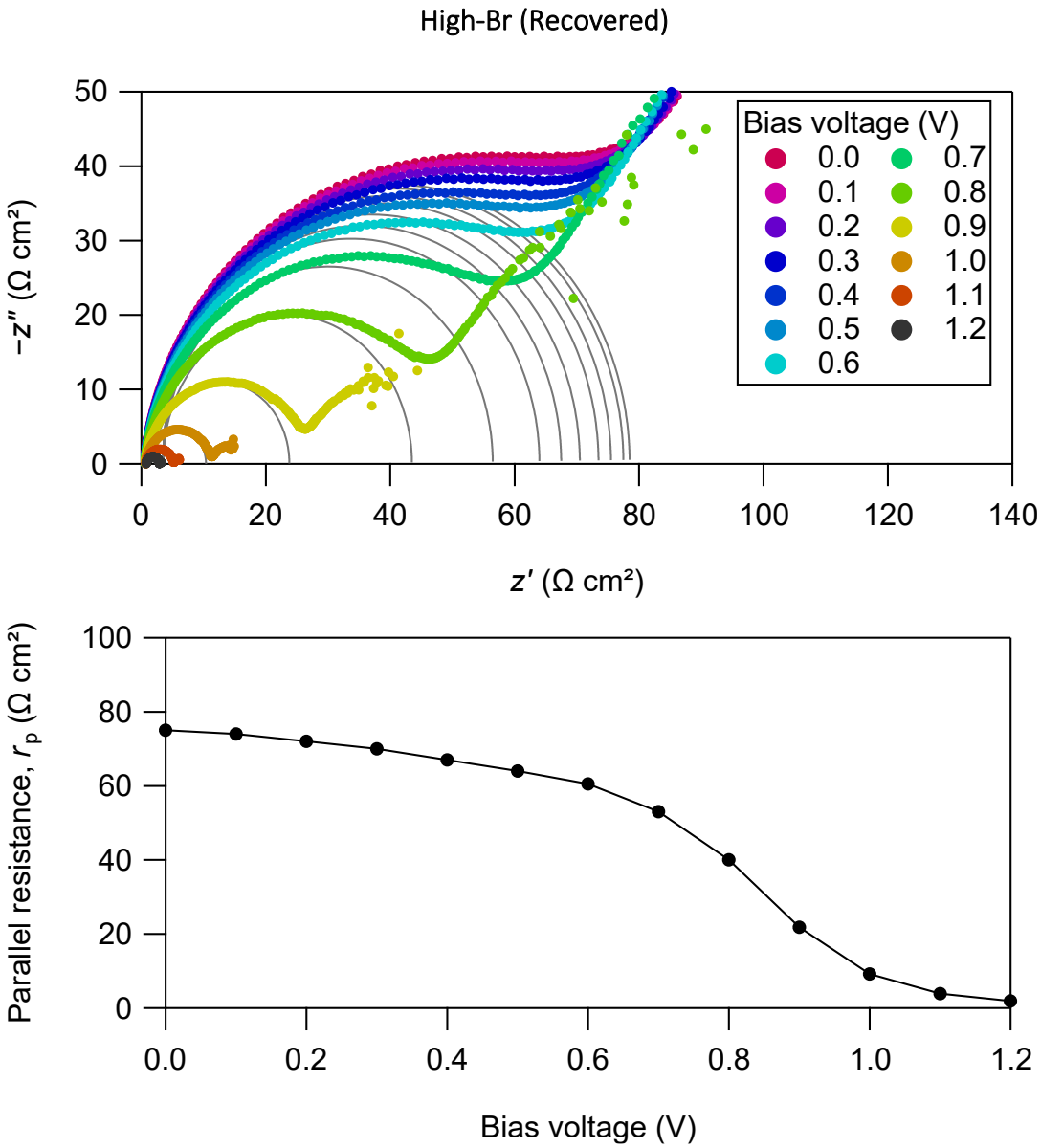
High-Br (Recovered)
Bias voltage (V)
0.0
0.1
0.2
0.3
0.4
0.5
0.6
0.7
0.8
0.9
1.0
1.1
1.2
−z″ (Ω cm²)
z′ (Ω cm²)
Parallel resistance, r_p (Ω cm²)
Bias voltage (V)

Appendix B: Light Intensity Dependence

Forward and reverse *J*–*V* scans were measured between −0.1 V and the open circuit voltage at a scan rate of 50 mV s^{-1} using a Keithley 2450 sourcemeter. The algorithm had a "soft return" feature such that the scan direction switched automatically to the reverse direction once the scan voltage exceeded V_{oc}. This prevents strong forward bias from being applied to the device, minimizing hysteresis.

J–*V* scans were measured as the light intensity was increased from less than 1/1000 sun to 1 sun. Attenuation was achieved by inserting neutral density filters combined with a variable aperture into the light path. The devices were operated for several minutes under AM1.5G before the measurement sequence began, and light exposure at each point was minimized. This helps maintain the device at a constant quasi-equilibrium state throughout the experiment. To keep the measurement times low, only *J*–*V* scans were measured: 300 s MPPT stability tests were not performed.

The J_{sc}, V_{oc}, PCE, and FF were determined for each scan direction and averaged together. *J*–*V* plots show the averaged data from the forward and reverse scans.

Data shown for the following devices and conditions:

Low-Br (Initial)

Low-Br (Transient)

Low-Br (Recovered)

High-Br (Initial)

High-Br (Transient)

High-Br (Recovered)

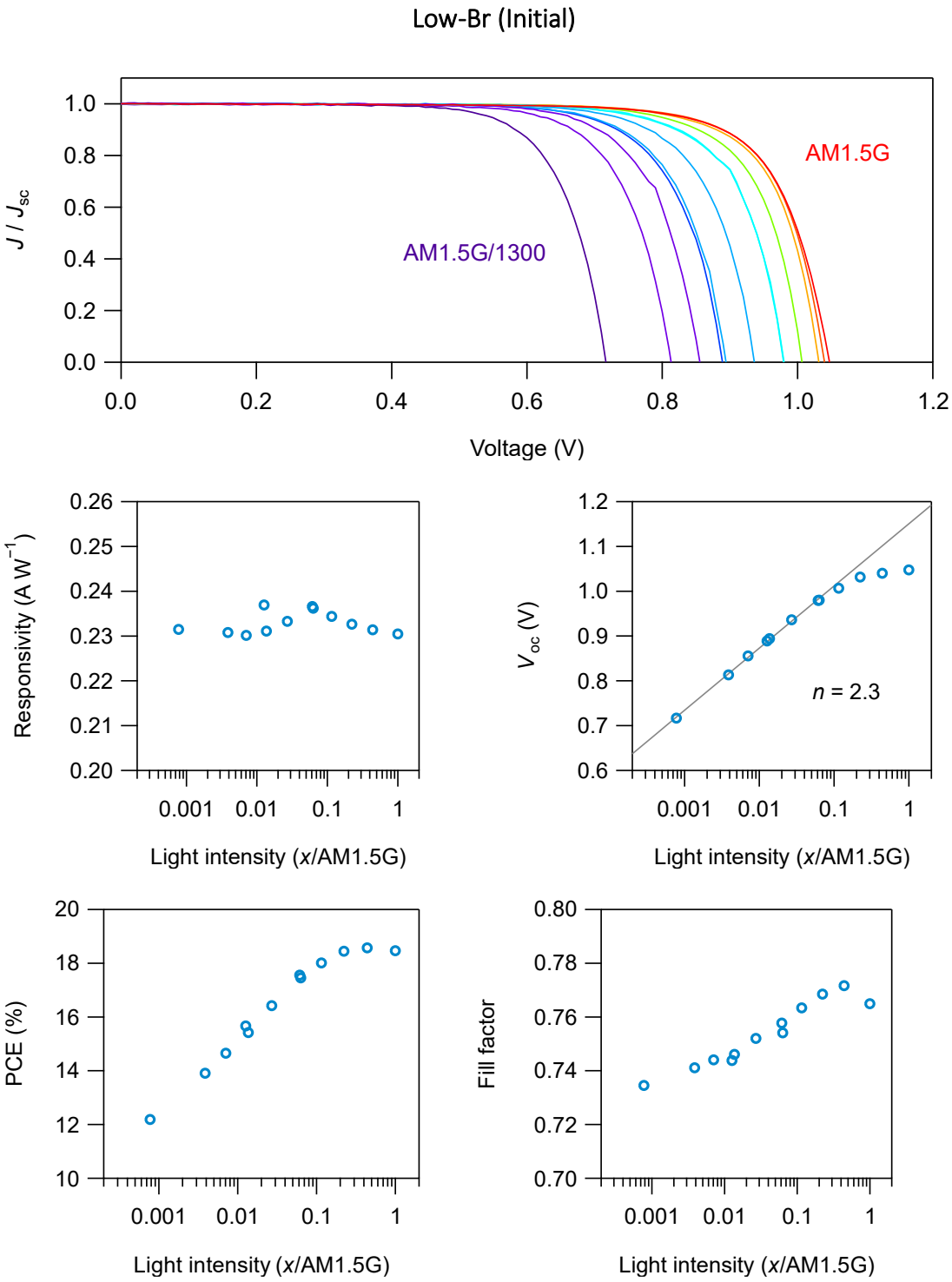
Low-Br (Initial)
J / J_sc
Voltage (V)
AM1.5G
AM1.5G/1300
Responsivity (A W^-1)
Light intensity (x/AM1.5G)
V_oc (V)
n = 2.3
PCE (%)
Fill factor

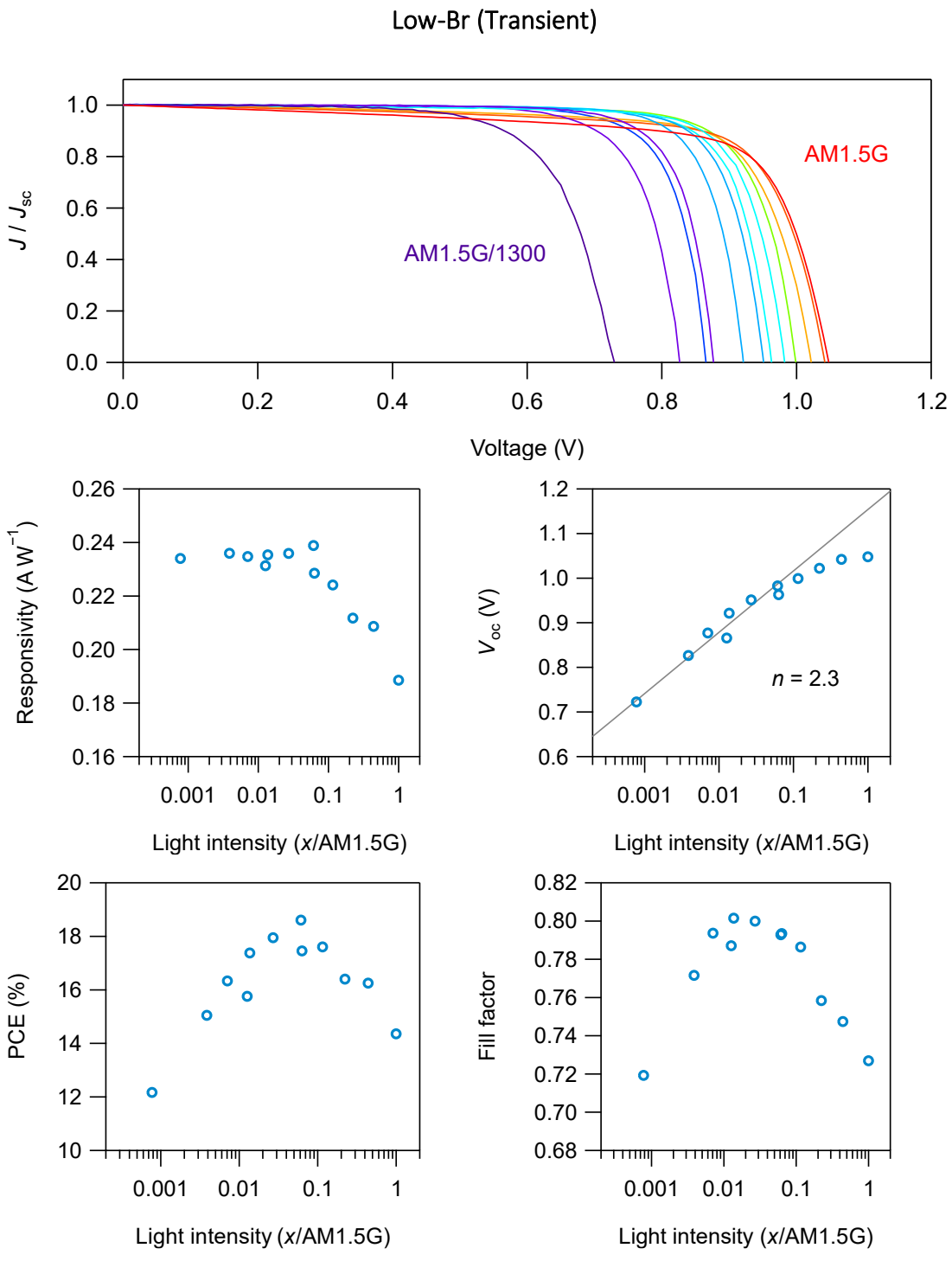
Low-Br (Transient)
J / J_sc
Voltage (V)
AM1.5G
AM1.5G/1300
Responsivity (A W^-1)
Light intensity (x/AM1.5G)
V_oc (V)
n = 2.3
PCE (%)
Fill factor

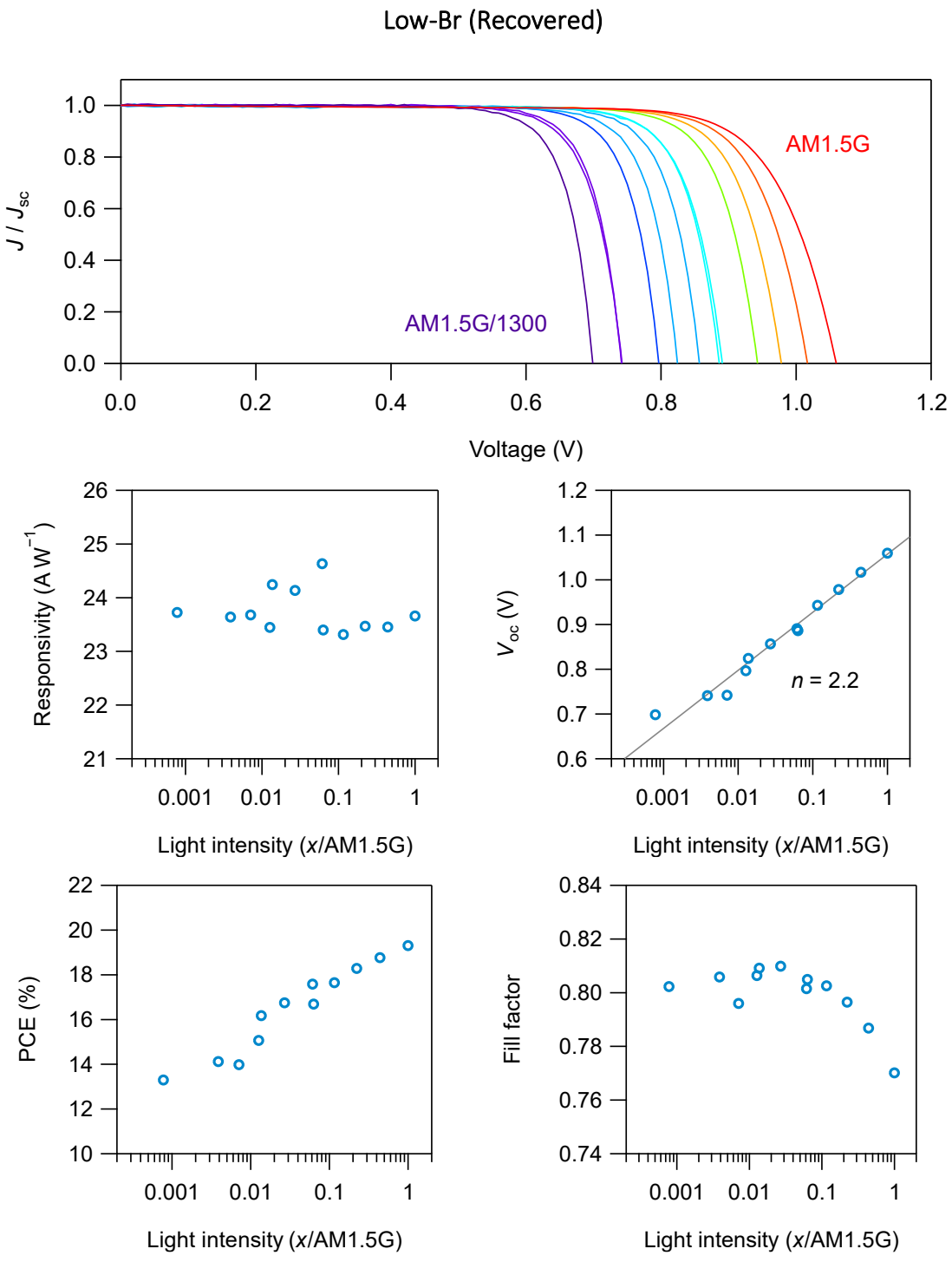
Low-Br (Recovered)
J / J_sc
AM1.5G
AM1.5G/1300
Voltage (V)
Responsivity (A W^-1)
Light intensity (x/AM1.5G)
V_oc (V)
n = 2.2
Light intensity (x/AM1.5G)
PCE (%)
Light intensity (x/AM1.5G)
Fill factor
Light intensity (x/AM1.5G)

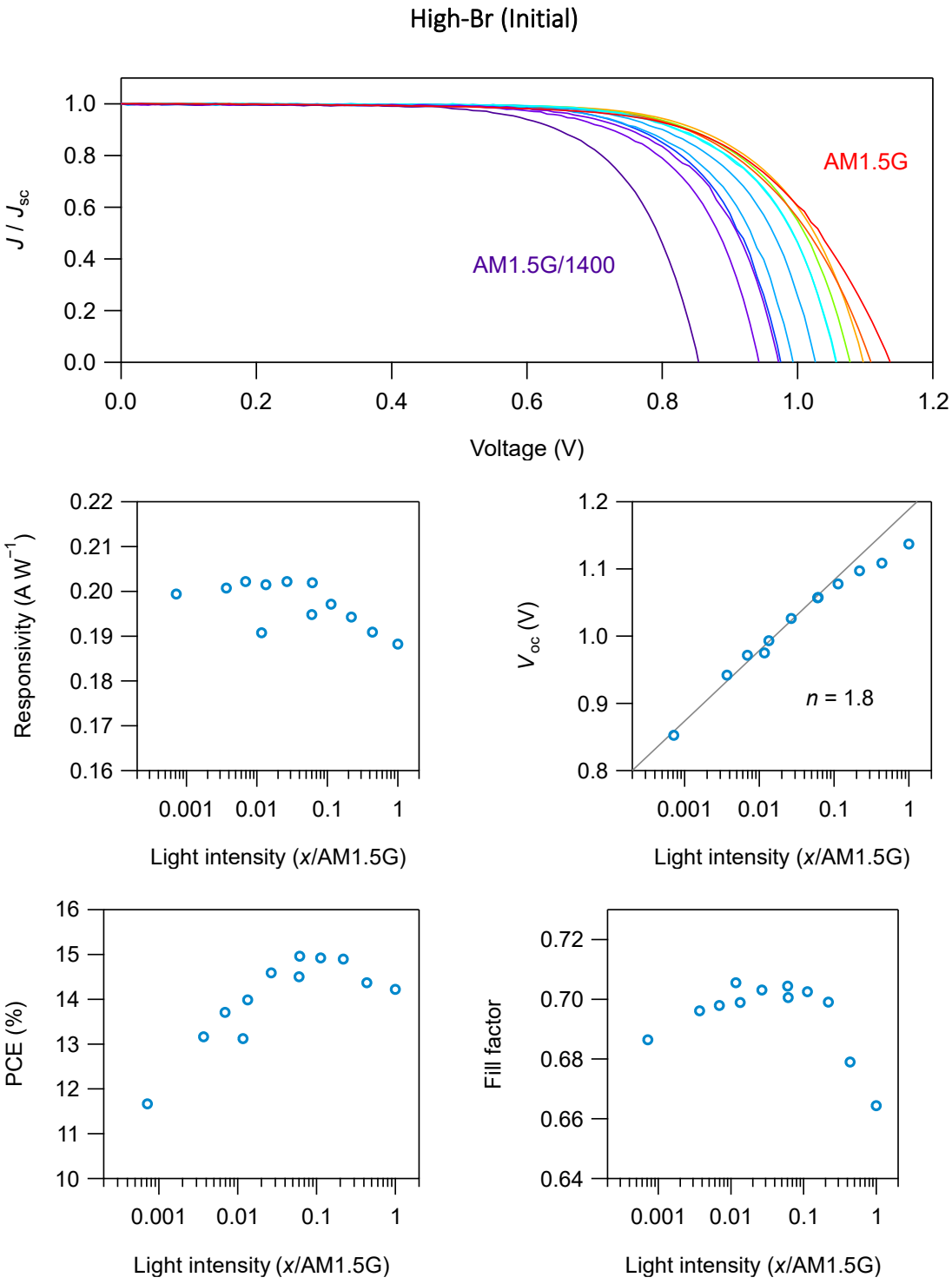
High-Br (Initial)
J / J_sc
Voltage (V)
AM1.5G
AM1.5G/1400
Responsivity (A W^-1)
Light intensity (x/AM1.5G)
V_oc (V)
n = 1.8
Light intensity (x/AM1.5G)
PCE (%)
Light intensity (x/AM1.5G)
Fill factor
Light intensity (x/AM1.5G)

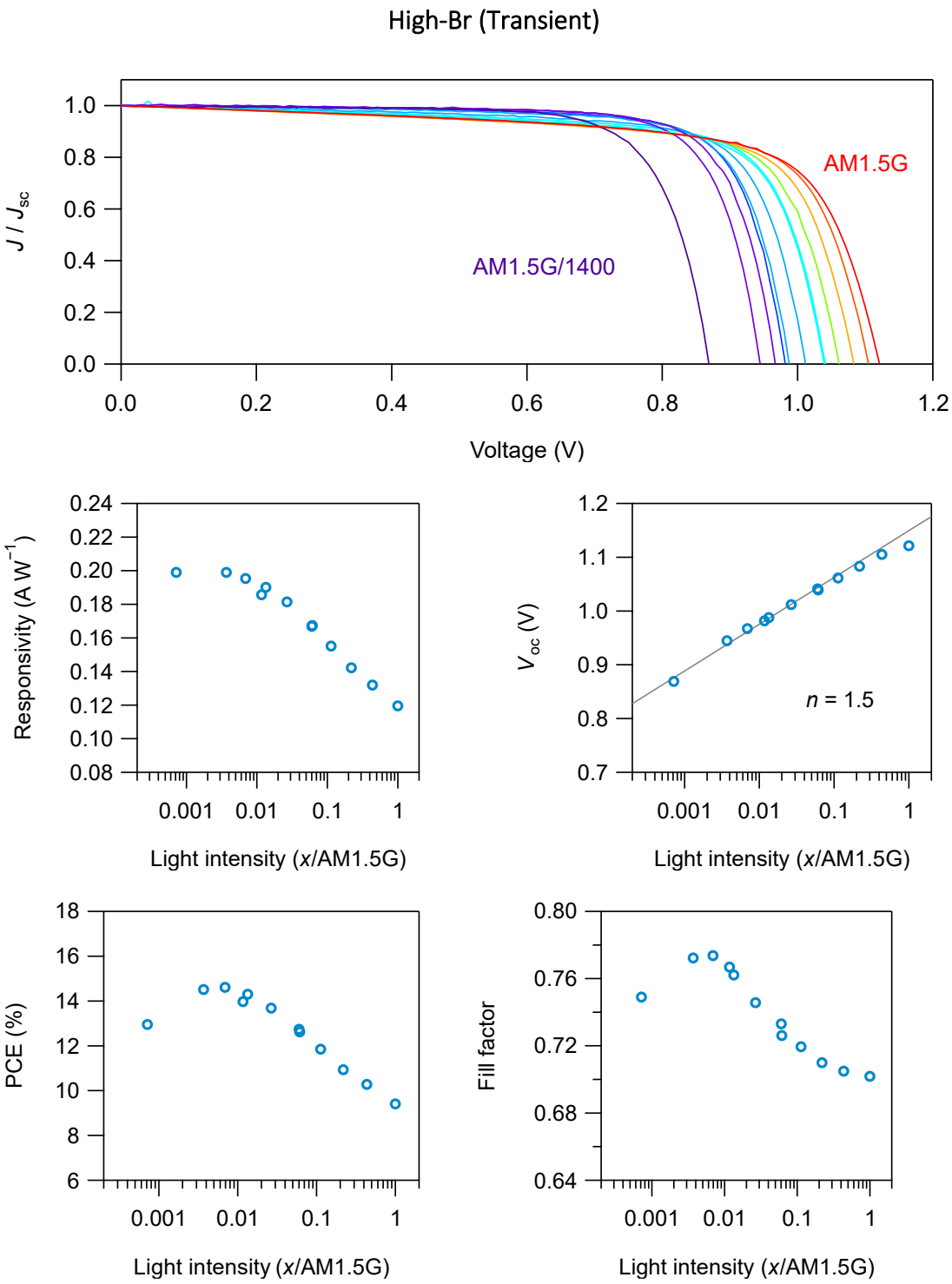
High-Br (Transient)
J / J_sc
Voltage (V)
AM1.5G
AM1.5G/1400
Responsivity (A W^-1)
Light intensity (x/AM1.5G)
V_oc (V)
n = 1.5
Light intensity (x/AM1.5G)
PCE (%)
Light intensity (x/AM1.5G)
Fill factor
Light intensity (x/AM1.5G)

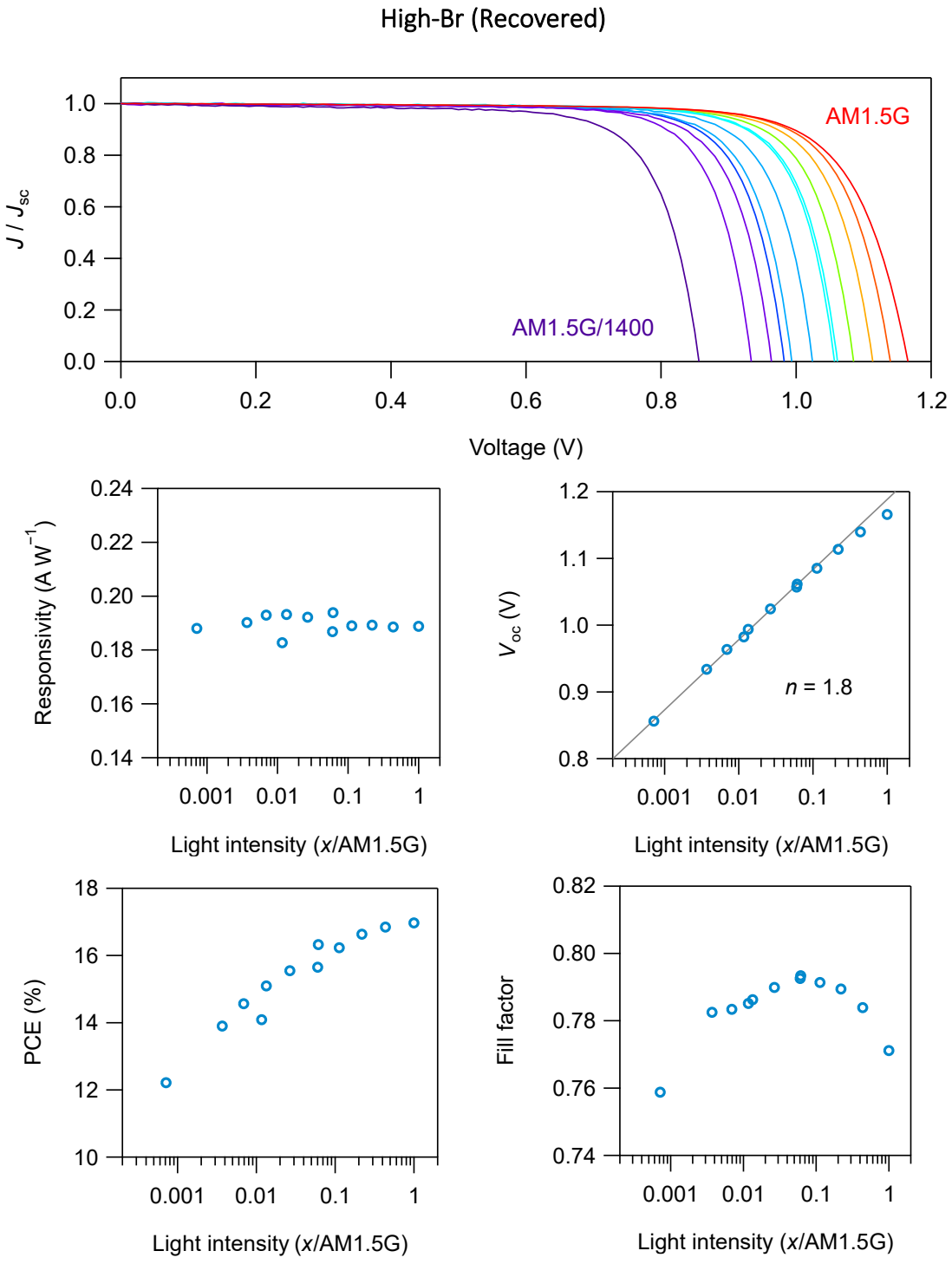
High-Br (Recovered)
AM1.5G
AM1.5G/1400
J / J_sc
Voltage (V)
Responsivity (A W^-1)
Light intensity (x/AM1.5G)
V_oc (V)
n = 1.8
PCE (%)
Fill factor